Probing photocurrent generation mechanisms in hybrid IR-senstive quantum dot/conjugated polymer solar cells

Elisabeth Strein

A dissertation

submitted in partial fulfillment of the

requirements for the degree of

Doctorate of Philosophy

University of Washington

2013

Reading Committee:

David S. Ginger, Chair

Samson A. Jenekhe

Xiaosong Scott Li

Program Authorized to Offer Degree:

Chemistry

University of Washington

Abstract

Probing photocurrent generation mechanisms in hybrid IR-senstive quantum dot/conjugated polymer solar cells

Elisabeth Strein

Chair of the Supervisory Committee:
Professor David S. Ginger
Chemistry

The work in this dissertation aims to improve the ability of hybrid polymer/quantum dot solar cells to harvest and utilize sunlight by contributing mechanistic insights into photocurrent generation. The mechanisms of charge transfer and energy transfer are explored spectroscopically in chapter three and both are found to contribute to photocurrent. Chapter four looks at excitation energy in excess of the bandgap and finds a rise in polaron yield which correlates with excess photon energy. Chapter two discusses details of the experimental techniques used to access the data discussed in the chapters that follow.

Chapter 1: Introduction

Why Solar Cells Matter

Sunlight is the most abundant renewable energy resource on earth. In about 53 minutes, the sun provides the earth with enough energy to meet global electricity demands for the year 2012.[1, 2] Despite the impressive power of the sun, only about 0.1% of the power supplied to address the energy consumption needs for 2012 was solar generated.[3]

Solar cells are devices that convert the energy in photons into electrical energy. The National Renewable Energy Lab (NREL) classifies solar cells into four broad categories[4]: multijunction cells, crystalline silicon (Si) cells, thin-film technologies (such as $Cu(In,Ga)Se_2$ or CdTe) and emerging photovoltaic (PV)s (see Figure 1). Emerging PV is further classified into the following subcategory types: dye-sensitized cells, organic cells, organic tandem cells, inorganic (CZTSSe) cells and quantum dot cells. The work in this dissertation falls into the emerging PV category and specifically concerns hybrid solar cells comprised of polymer/quantum dot blends, bridging NREL's organic and quantum dot cell categories.

Incentives for Emerging PV

As clearly indicated on the NREL record efficiencies chart (Fig 1), emerging PV cells (denoted in red) are the least efficient variety of solar cell. The inefficiencies arise from inherent material properties which impact the fundamental device physics processes (and species) involved to generate and extract carriers.[5] Rather than generating free carriers directly when under illumination, both organic and quantum dot cells generate excitons—or Coulombically bound electron-hole pair species.[6] Consequently, additional trap and recombination pathways are opened within the low dielectric organic environment[7] and the carrier confinement seen in the quantum dots;[8] and additional conditions must be met in order for the "first step", free carrier generation, to occur in these devices.[5, 6, 9]

The emerging PV cells however possess several important characteristics that give rise to notable advantages over their more efficient counterparts. They have the potential to significantly reduce unit costs, allowing solar cell technologies to become market competitive with other energy sources.[10] They can be produced from ink in a roll-to-roll fashion.[10, 11] This large area/high yield manufacturing processes can potentially capitalize on the equipment, infrastructure, expertise and maturity of the printing industry. They have a projected production capacity of 1 GW per day, which scales with the level of projected global energy demand.[10] Emerging PV have thin active areas of 50-200 nm, which in addition to the advantage of cost reduction also are beneficial to the environment in terms of minimizing waste and overall material demands.[11] Finally they can have energy payback times (EPBT, understood to be the time it takes to earn back the energy invested in its creation) as low as one day, which marks a distinct improvement over the 1-2 year EPBT for crystalline Si cells.[10]

Hybrid Solar Cells

The vision for the hybrid polymer/quantum dot solar cells studied in the bulk of this dissertation is to make devices that harvest a larger portion of solar irradiation than is possible in polymer/fullerene blends.[12] Although it is possible to improve device net responsivity by tailoring polymer/polymer blends to extend the spectral range, these devices are inherently limited by significant geminate recombination due in part to the aforementioned low dielectric constants inherent to polymers.[13, 14] To this end, polymer/quantum dot hybrids are promising because the quantum dots provide a high dielectric route to increase photovoltaic spectral range.

It should be duly noted that as the spectral harvesting range is extended into the IR region, a single junction solar cell will see decreased open circuit voltage (V_{oc}) limited by the energy absorbed by the low bandgap material.[15, 16] Consequently, in practical applications the polymer/QD blends discussed in this dissertation would be best used as a layer in a tandem cell. (See Figure 2 for a cross sectional TEM image of an actual polymer/quantum dot device. Devices studied in chapter three follow the device structure imaged in Figure 2.)

Quantum dots

Basic Properties

Within the environment of a semiconducting crystal lattice, it is energetically favorable for an electron wavefunction to be delocalized over a length scale commonly referred to as the Bohr radius. Of note for this dissertation, in the specific case of a bulk PbS crystal lattice, the Bohr radius is about 18 nm.[17] Quantum dots are 3D semiconducting crystal lattices that terminate within this length scale; the PbS quantum dots used in this dissertation ranged from 2-5 nm in diameter. Electron wavefunctions within this environment are consequently constrained in terms of location and energy. Since the electron energy is no longer free to assume any arbitrary value, we say that it is quantized. Formally, this is approximated by assuming the potential of a particle-in-a-sphere

$$V = \begin{cases} 0 & r < R \\ \infty & r > R \end{cases} \tag{1.1}$$

Using the work done by Flügge[18] the solution to the Schrödinger equation is found as

$$\Phi_{n,\ell,m}(r,\theta,\phi) = A\frac{Y_\ell^m(\theta,\phi)j_\ell\left(k_{n,\ell}r\right)}{r} \tag{1.2}$$

Where A normalizes the wavefunction, $Y_\ell^m(\theta,\phi)$ is the spherical harmonic, and $j_\ell\left(k_{n,\ell}r\right)$ is the ℓ^{th} order spherical Bessel function, where $k_{n,\ell} = \alpha_{n,\ell}/R$ and $\alpha_{n,\ell}$ is the nth zero of j_ℓ.

The allowed energy states associated with this solution are

$$E_{n,l} = \frac{\hbar^2 k_{n,\ell}^2}{2m_o} = \frac{\hbar^2 \alpha_{n,\ell}^2}{2m_o R^2} \propto \frac{1}{R^2} \tag{1.3}$$

Equation 1.3 demonstrates both that energy is quantized and that that it is inversely proportional to the square of the radius.

A quantum dot, obviously is not a sphere with V=0 within its boundaries, but the particle-in-a-sphere model is still informative. When a carrier is excited in a quantum dot we can use the effective mass approximation derived from Bloch's theorem which looks at wavefunction behavior within the periodicity of a crystal lattice to approximate the energy of the conduction and valance bands as[19]

$$E_k^c = \frac{\hbar^2 k^2}{2m_{eff}^c} + E_g \tag{1.4}$$

$$E_k^v = \frac{-\hbar^2 k^2}{2m_{eff}^v} \tag{1.5}$$

The effective mass provides a way account for the complexity of the periodic potential felt by carrier in the semiconductive lattice, allowing the carriers to be treated as if they see the same potential as free particles. Thus behave similarily to what was found in equation 1.3—only they have a different mass.[20]

It is important to realize that even though the effective mass approximation allows us to capitalize on the particle-in-a-sphere treatment, these excited carriers do not behave at all as free carriers. The electron and hole are bound together in the quantum dot as an electron-hole pair due to Coulomb exchange interactions between them[19, 21]. Thus, in order to generate current from photoexcited quantum dots, an energetic landscape must exist that drives the separation of the exciton.

Ligands and Traps

The immediate energetic environment surrounding the quantum dot crystal lattice is made of the ligands attached to the quantum dot surface (see Figure 3) and surface "trap" states. These factors play a critical role in creating functional devices.

As synthesized, the PbS quantum dot surface is stabilized with an oleate capping layer, the use of which controls nucleation and growth during synthesis, leads to a narrow size distribution, and provides chemical and colloidal stability.[22] Furthermore, they dictate the interparticle spacing. Both the length and the lack of conjugation on the long chained oleate make this ligand an effective electrical insulator. The resulting "barrier" must be replaced with shorter ligands more conducive to electrical transport.[23]

The PbS quantum dots used in this dissertation underwent two separate ligand exchanges. The first was solution based and involved exposing the as-synthesized quantum dots to a large excess of competitive target ligand, which in my case was always butylamine. The exchange typically was extended over and hour and repeated two times to maximize the removal of the oleate.

The second exchange took place post-film fabrication. Competitive ligand solution covered the film for under a minute and was subsequently removed. I observed a decrease in the interparticle distance and an increase in device current with films that underwent this second treatment. TEM microscope images suggest a significant quantum dot reordering takes place throughout the film during this exchange (see Figure 4). This rearrangement is also witnessed by film cracking.

In addition to the morphological changes invoked through the ligand exchange process, it is also possible for ligand exchanges to impact the surface dipole--and consequently change the conduction and valance band energy levels.[24] This is important to consider because changes to the state band diagram can have significant repercussions on device performance.

The state band diagram can also undergo significant revision due to trapping.[3] Traps states arise with slight defects in the quantum dots such as vacancies, impurities within the crystal lattice, or unwanted surface adsorbates.[25] They can lead to device instabilities coupled with a severe reduction in net photocurrent generation.

Ligands and traps both underscore the importance of the environment that the quantum dots interact with. This is to be expected given the ratio of surface area to volume for quantum dots.

Chapter introductions:

With this brief contextual background for my work, I conclude this introduction by introducing the chapters that will follow. Chapter 2 discusses the workhorse experiments I conducted to characterize my devices: external quantum efficiency measurements, current vs voltage sweeps taken in both the dark and under illumination, photoluminescence excitation, and finally photoinduced spectroscopy. Chapter 3 discusses experiments I did looking at charge transfer and energy transfer in the polymer/quantum dot devices, where I ultimately found that both mechanisms can effectively generate photocurrent within the devices. Chapter 4 discusses a study on polaron generation as the sample is excited by varying photon energies and demonstrates that “hot” holes are able to produce increased polaron populations.

Figures for Chapter 1

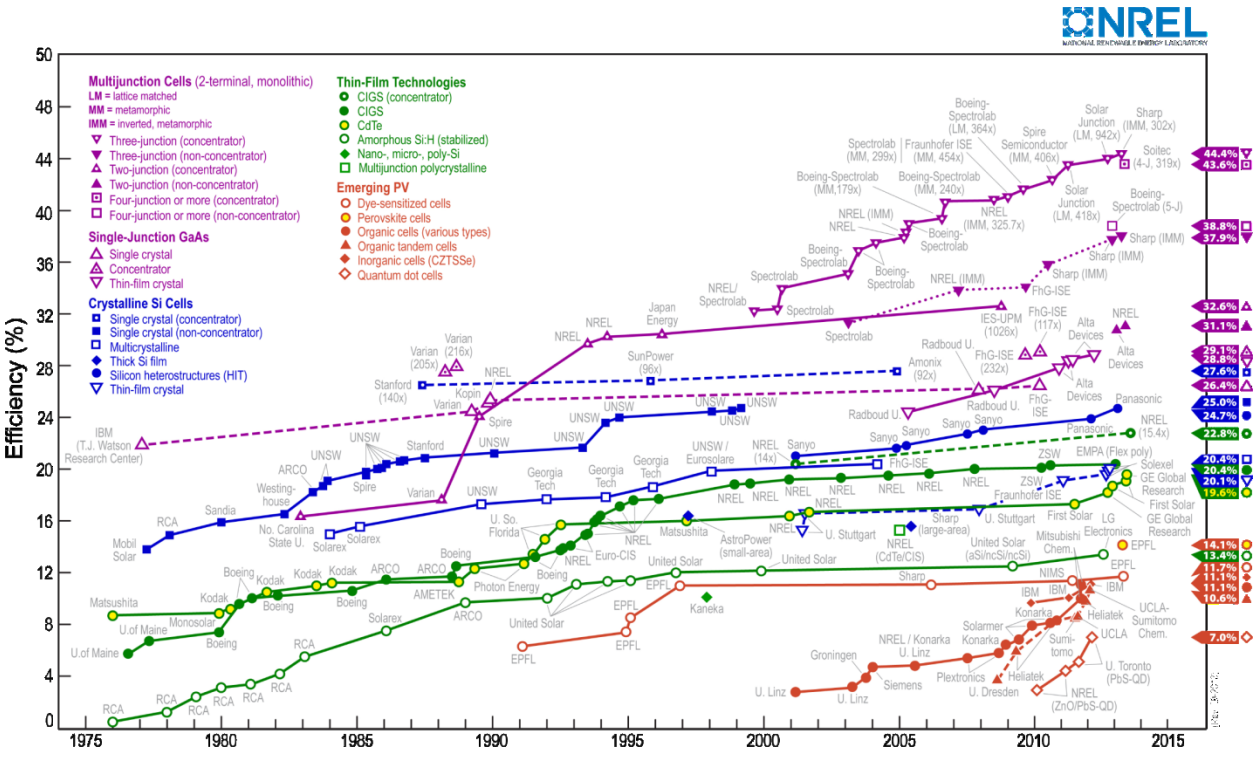

Figure 1 NREL "Best Research-Cell Efficiencies" for turning light power into electrical power are listed as a function of when the device was tested. Solar cells are distinguished categorically: multijunction cells (purple), crystalline silicon (Si) cells (blue), thin-film technologies(green) and emerging PV (red). This chart is free and open to the public and can be found on the NREL site http://www.nrel.gov/ncpv/

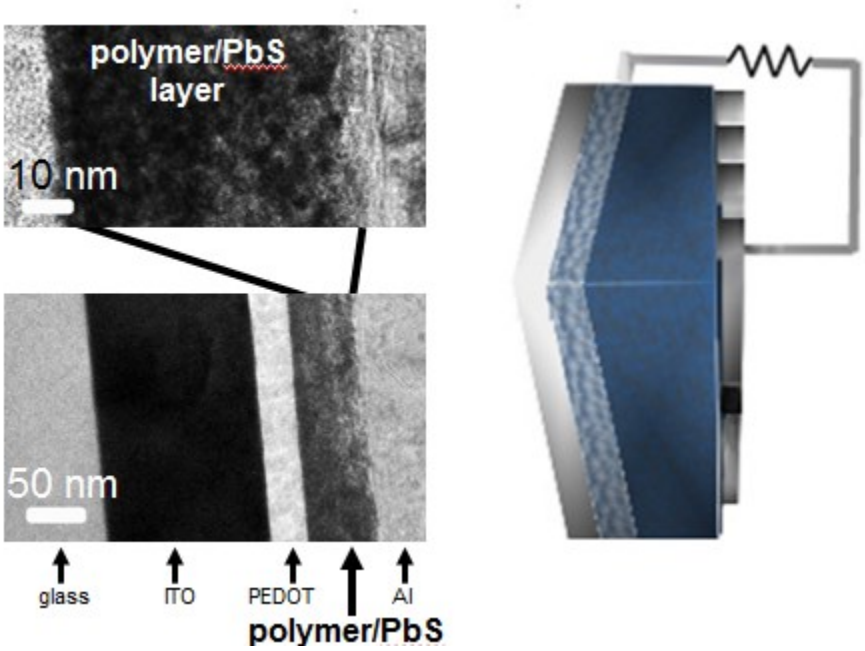

Figure 2 Cross-sectional TEM images of a polymer/quantum dot device on the left with the corresponding cartoon of an entire device on the right.

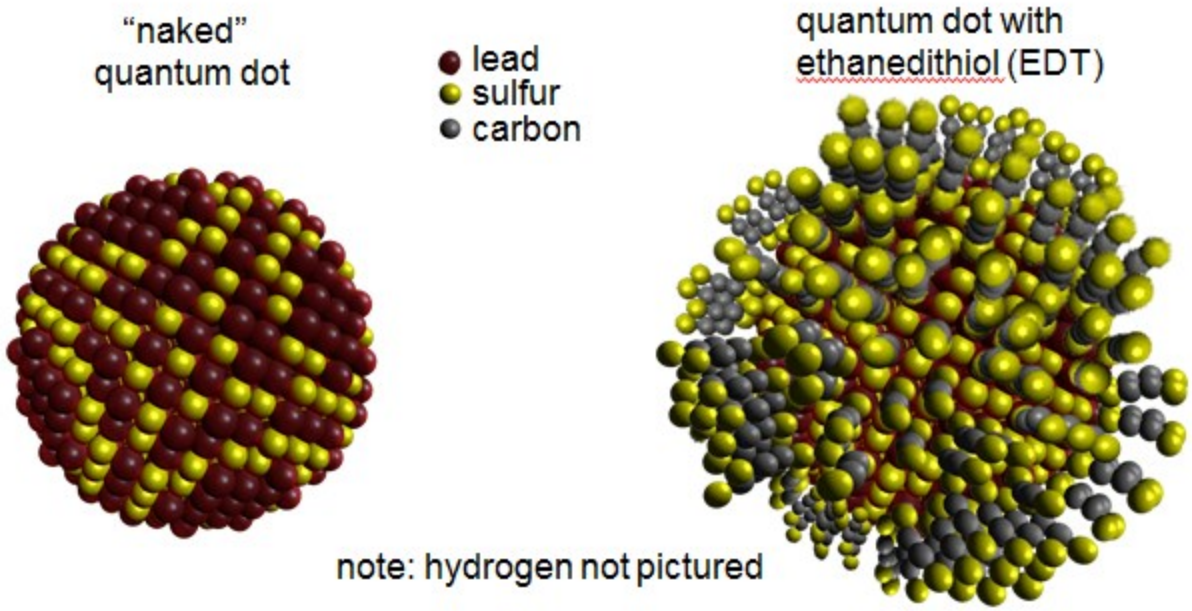

Figure 3 depicts a PbS quantum dot. On the left the depiction does not include any ligands. On the right is shown a cartoon of the EDT ligand covering the quantum dot surface.

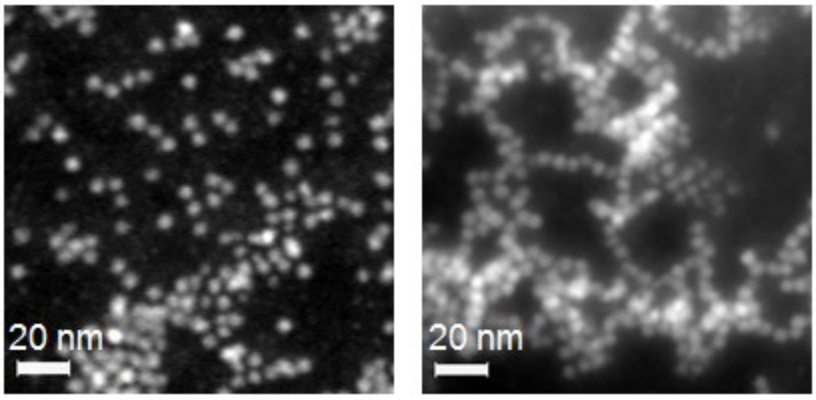

Figure 4 TEM images of a highly diluted PbS/polymer blend solution drop cast onto a TEM grid . In the image on the left, the quantum dots have been butylamine treated. In the second image the film was further treated with ethanedithiol (EDT) solution. The images indicate that is it possible for quantum dots in the film to rearrange during the ligand treatment process.

1. World energy consumption, 1990-2012 U.S. Energy Information Administration (EIA), International Energy Statistics database (as of July 2013), www.eia.gov/forecasts/ieo/index.cfm.
2. Solar Irradiance Data, National Oceanic and Atomspheric Administration (NOAA). (accessed Oct 2013) www.ngdc.noaa.gov/stp/solar/solarirrad.html
3. E. H. Sargent, *Nature Photonics*, 2012, **6**, 133-135.

4. "Best Research Cell Efficiencies" (May 2013). National Renewable Energy Laboratory, 2013. (accessed Oct, 2013) www.nrel.gov/ncpv/
5. T. M. Clarke and J. R. Durrant, *Chemical Reviews*, 2010, **110**, 6736-6767.
6. J.-L. Brédas, J. E. Norton, J. Cornil and V. Coropceanu, *Accounts of Chemical Research*, 2009, **42**, 1691-1699.
7. P. K. Nayak, K. L. Narasimhan and D. Cahen, *Journal of Physical Chemistry Letters*, 2013, **4**, 1707-1717.
8. H. W. Hillhouse and M. C. Beard, *Current Opinion in Colloid & Interface Science*, 2009, **14**, 245-259.
9. A. E. Jailaubekov, A. P. Willard, J. R. Tritsch, W. L. Chan, N. Sai, R. Gearba, L. G. Kaake, K. J. Williams, K. Leung, P. J. Rossky and X. Y. Zhu, *Nature Materials*, 2013, **12**, 66-73.
10. N. Espinosa, M. Hosel, D. Angmo and F. C. Krebs, *Energy & Environmental Science*, 2012, **5**, 5117-5132.
11. S. B. Darling and F. You, *RSC Advances*, 2013, **3**, 17633-17648.
12. Y. Yao, C. J. Shi, G. Li, V. Shrotriya, Q. B. Pei and Y. Yang, *Applied Physics Letters*, 2006, **89**.
13. C. Groves, J. C. Blakesley and N. C. Greenham, *Nano Letters*, 2010, **10**, 1063-1069.
14. A. Gonzalez-Rabade, A. C. Morteani and R. H. Friend, *Advanced Materials*, 2009, **21**, 3924-+.
15. R. A. J. Janssen and J. Nelson, *Advanced Materials*, 2013, **25**, 1847-1858.
16. M. C. Scharber, D. Wuhlbacher, M. Koppe, P. Denk, C. Waldauf, A. J. Heeger and C. L. Brabec, *Advanced Materials*, 2006, **18**, 789-+.
17. C. Burda, X. Chen, R. Narayanan and M. A. El-Sayed, *Chemical Reviews*, 2005, **105**, 1025-1102.
18. S. Flugge, *Practical Quantum Mechanics*, Springer, Berlin, 1971.
19. T. Hanrath, *Journal of Vacuum Science & Technology A*, 2012, **30**, -.
20. J. N. David, in *Nanocrystal Quantum Dots, Second Edition*, CRC Press, 2010, pp. 63-96.
21. J. Y. Kim, O. Voznyy, D. Zhitomirsky and E. H. Sargent, *Advanced Materials*, 2013, **25**, 4986-5010.
22. D. V. Talapin, J.-S. Lee, M. V. Kovalenko and E. V. Shevchenko, *Chemical Reviews*, 2009, **110**, 389-458.
23. K. S. Jeong, J. Tang, H. Liu, J. Kim, A. W. Schaefer, K. Kemp, L. Levina, X. Wang, S. Hoogland, R. Debnath, L. Brzozowski, E. H. Sargent and J. B. Asbury, *ACS Nano*, 2012, **6**, 89-99.
24. P. R. Brown, J. Jean, D. Wanger, T. P. Osedach, N. Zhao, R. Lunt, M. G. Bawendi and V. Bulovic, Engineering Energy Level Alignment in PbS QD Photovoltaics Through Ligand Exchange (poster), Ventura, CA 2013.
25. K. S. Jeong, J. Tang, H. Liu, J. Kim, A. W. Schaefer, K. Kemp, L. Levina, X. H. Wang, S. Hoogland, R. Debnath, L. Brzozowski, E. H. Sargent and J. B. Asbury, *Acs Nano*, 2012, **6**, 89-99.

Chapter 2: Experimental Methods

As my research concerns itself primarily with solar cells, in this chapter I discuss the ways I characterized the response of both materials and devices to incident light, namely through external quantum efficiency (EQE) spectral measurements, light IV curves, photoluminescence excitation (PLE) spectra and photoinduced absorption (PIA) measurements. As PIA is a somewhat lesser known technique, I also provide some of its theoretical/mathematical underpinnings.

As a global note, all measurements were taken under dynamic vacuum or in a glovebox.

EQE measurement

For a given incident illumination wavelength, EQE measurements demonstrate what percent of incoming photons were converted to current. Spectra were generated with a tungsten halogen lamp equipped with a monochromator. The resulting current was measured with a Keithley 2400 and data were calibrated to the response of a Si photodiode with known responsivity.

IV curves

IV curves plot the current measured in a device while a bias voltage is swept. IV data confirm that a solar cell has a diode response and light IV data demonstrate that upon illumination the device produces a current. In order to accurately rate device IV performance to other cells, the measurement needs to be taken under standard reporting conditions with 1000 $\frac{\mathrm{W}}{\mathrm{m}^2}$ irradiance and using the AM 1.5 global reference spectrum rather than illumination with light from a single wavelength.[1] By way of explanation, "AM" is an abbreviation for the air mass coefficient. AM0 is the sun's spectrum outside of earth's atmosphere and is useful for solar panels used in space. AM1 is the spectrum received on earth after traveling through the atmosphere when solar zenith is zero (or in other words, when the sun is directly overhead). If, rather than being directly overhead, the sun is at an angle, the light will have a longer path to travel through the atmosphere before it reaches the earth. Consequently, the standard is to use the AM1.5 spectrum that represents the overall yearly average air mass coefficient. This has been determined to be at a solar zenith of 48.2°.[2]

In practice, a solar simulator was used to generate light IV data. Current measurements with a Keithly 2400 are used to determine both the solar simulator power settings and the position of the device with respect to the light. For each device I used two different calibration methods to determine device positioning relative to the solar simulator prior to collecting IV data. For one, the appropriate position was located by measuring the current through the device and adjusting position until the current matched the anticipated theoretical current calculated from device EQE measurements. This positioning sometimes had to be approximated because the current through the devices was not always constant with time. Sometimes the intense solar simulator light would result in device degradation and the current would drop over time, ultimately resulting in a lower EQE response than what we used for calibration. Other times the light energy improved device performance with time—it is possible this was due to some mild annealing that occurred under the heat of the solar simulator light output; also it is

possible that over time the photon flux caused trap states in the device to be filled and consequently there was an increase in number of collected carriers. Device instability in either case could make it challenging to use the device to calibrate proper positioning. The other method of calibration made use of current through a calibrated Si photodiode to determine the appropriate positioning. It was useful in some respects in that it provided consistent illumination fluence, but unfortunately due to spectral mismatch from the responsivity of the device as compared to that of the Si calibration diode, it did not represent 1000 $\frac{\mathrm{W}}{\mathrm{m}^2}$ AM1.5 illumination for the devices.[1]

Photoluminescence Excitation (PLE) Spectroscopy

PLE spectra result when photoluminescence (PL) from the sample is collected while the sample is spectrally excited. In the case of polymer/quantum dot blends, the technique was used to selectively monitor quantum dot PL by placing an appropriate long pass filter before the detector which isolated the collected signal from any polymer PL signal. Although this is a routine technique, for the IR detection sensitivity required for my samples, it was not possible to use any existing fluorometers at the University of Washington. Consequently I wrote a LabView program and designed a simple optical set up as follows: a monochromated tungsten halogen lamp was used as the excitation source and sample photoluminescence intensity was monitored with a Si/InGaAs dual-band photodetector (ThorLabs, DSD2)equipped with the appropriate long pass filter. Emitted light was wave-guided from the side of the glass substrate and focused using two aspheric lenses mounted in front of the photodetector. A fraction of the excitation light was split with a glass microscope slide to monitor the excitation intensity with an amplified silicon ($\lambda <= 1000$ nm) or an amplified InGaAs ($\lambda > 1000$ nm) photodetectors. All spectra were normalized to the measured excitation intensity. For a schematic of the PLE experiment, see figure 1.

In my specific research I used PLE spectra to determine if energy transfer was a possible mechanism for photocurrent generation for a specific polymer/quantum dot blend.

Photoinduced Absorption (PIA) Spectroscopy

PIA is a pump-probe technique used to determine if excited state populations with micro-to-millisecond lifetimes are formed as a result of photoexcitation (for schematic see figure 2). For polymer/quantum dot blends, the formation of a polaron (or a charged species and its surrounding environment) on the polymer is indicated by PIA signal at energies lower than the bandgap of the material. If the polymer has either donated an electron or accepted a hole, the resulting positive charge on the polymer causes a restructuring of the conjugation along the polymer backbone that is observed spectrally as an opening of states below the bandgap of the polymer.

A classic reference for electronic processes in conductive organic polymers by Pope and Swenberg treats the hole on the polymer as a quasiparticle and provides a concise description of the PIA state that I quote directly as follows:

> Since these quasiparticles represent defects, they occupy special energy levels within the energy gap of the neat polymer. For the polarons, there are two levels, one for the hole and another for the electrons. These levels are split off from the valence and

> conduction band respectively, so the lower level is normally doubly occupied and the upper level is unoccupied. […] When the Fermi level and band gap are formed so that there is symmetry between valence and conduction bands […], the positive and negative polaron levels will be equally spaced from their respective parent bands.[3] (pg 866-867)

By using low energy wavelengths to probe the excited system we are able to measure whether or not there is sub-bandgap absorption. If the excited polymer/quantum dot blend proves to be sensitive to the probe, we ascribe this sensitivity to the polaronic states. In practice, PIA signal is detected as a change in transmission scaled to the total transmission and since the polaron causes the light to be lost to absorption, the signal is recorded as negative.

Experimental details

Standard lock-in techniques[4, 5] were used to obtain PIA data and consequently all pump illumination on the sample was modulated. I pumped using chopped light from an LED that was either modulated electrically (using an Agilent 33120A waveform generator) or mechanically (using a chopper wheel). With the exception of the modulation dependent data, the sample was typically pumped with 200 Hz modulated light, probed using a monochromated tungsten halogen lamp, and the resulting signal was collected with a Si/InGaAs dual-band photodetector (Thorlabs, DSD2) equipped with a monochromator and a longpass filter to isolate the signal from the pump light. For modulation dependent data, the pump modulation was swept from 20 to 10000 Hz and the signal was collected with an amplified Si detector (Thorlabs, PDA36A).

Prior to making a measurement, the longpass filter was temporarily removed and the detector measured signal from the pump so that the lock-in could be phased to the chopping frequency of the pump. Since the phase indicates the period of chopping frequency, it provides an electrical reference for the pump's photoexcitation of the sample. Consequently, the phasing allows signal related to the sample to be disentangled from all other activity in the detection circuitry. The lock-in reports this signal in two parts: the in-phase data indicate any detectable signal within one period; the quadrature data indicate any signal which lasted longer than one period. For 200 Hz modulation, the chopping period is 5 ms the—or more explicitly, pump light is exciting the sample for 2.5 ms and then there is no pump illumination for 2.5 ms. In-phase data is signal detected within the 5 ms period (the sine component of the signal) and the quadrature is signal that lasts longer than 5 ms (or the cosine component of the signal). Quadrature signal is inverted from in-phase signal: the corollary to negative in-phase signal is positive quadrature signal. Although I always collected both the in-phase and quadrature signals, data presented in this dissertation is typically in-phase only unless otherwise noted.

As the probe wavelength is varied we generate a spectral fingerprint of the sub-band gap states made available when the polaron has caused conjugation shifts along the polymer backbone. We, further, can use PIA to go several steps beyond a basic spectrum. We can use PIA to determine the dependency of a long-lived excited state population to frequency of excitation, the intensity of the excitation, and excitation energy. These relationships respectively allow access to polaron lifetimes and decay dynamics, bimolecular and monomolecular recombination processes, and hot carrier activity in the

blends. I will save the discussion concerning pump energy variations for chapter 4, but will discuss the impact of varying the pump intensity and chopping frequency below in the following section.

PIA Theoretical Foundations

A book chapter by Wohlgenannt, Ehrenfreund and Vardeny gives a thorough look at the theory underpinning the information contained within PIA data.[5] Here I provide a summary of their analysis and direct the interested reader to their writing for further details.

In a PIA experiement, the pump light provides a photon flux which generates some photoexcitation population density N(x,t), which could give rise to polaron formation and consequently result in variations in $\Delta\alpha(\mathrm{E},\mathrm{x},\mathrm{t})$, the sample's absorption. The photoexicted population density is directly proportional to the changes in absorption and are related by σ, the cross-section for absorption.

$$\Delta\alpha(\mathrm{E},\mathrm{x},\mathrm{t}) = \sigma(\mathrm{E})\mathrm{N}(\mathrm{x},\mathrm{t}) \tag{2.1}$$

where E is photon energy, x is position in the sample and t is time. Formally, the $\frac{\Delta\mathrm{T}}{\mathrm{T}}$ PIA signal is related to changes in absorption by

$$\frac{\Delta\mathrm{T}}{\mathrm{T}}(\mathrm{E},\mathrm{t}) = 1\text{-}\mathrm{e}^{\left(-\int_0^{\mathrm{d}}\Delta\alpha(\mathrm{E},\mathrm{x},\mathrm{t})\mathrm{dx}\right)} \tag{2.2}$$

where d is the total thickness of the sample. In practice we measure a signal that is on the order of parts per million and probe thin (50-150 nm thick) samples which exhibit relatively low optical density, so it is reasonable to assume that $\frac{\Delta\mathrm{T}}{\mathrm{T}} \ll 1$ and $\alpha\mathrm{d} \ll 1$

$$\frac{\Delta\mathrm{T}}{\mathrm{T}}(\mathrm{E},\mathrm{t}) \cong \Delta\alpha\mathrm{d} \qquad \text{or} \qquad \frac{\Delta\mathrm{T}}{\mathrm{T}}(\mathrm{E},\mathrm{t}) \cong \sigma(\mathrm{E})\mathrm{N}(\mathrm{x},\mathrm{t}) \tag{2.3}$$

With these reasonable assumptions we thus approximate PIA signal as being directly proportional to the excited state population density N.

This is an important relationship in part because both monomolecular and bimolecular recombination processes are described mathematically in terms of changes to the net excited state population in time as dictated by the the population that has been annihilated by recombination subtracted from population initially generated by the incident light.

$$\frac{\mathrm{dN}(\mathrm{t})}{\mathrm{dt}} = \mathrm{gI_L}(\mathrm{t})\text{-}\beta\mathrm{N}(\mathrm{t}) \quad \text{(monomolecular)} \tag{2.4}$$

$$\frac{\mathrm{dN}(\mathrm{t})}{\mathrm{dt}} = \mathrm{gI_L}(\mathrm{t})\text{-}\gamma\mathrm{N}^2(\mathrm{t}) \quad \text{(bimolecular)} \tag{2.5}$$

where g is the generation rate constant, $\mathrm{I_L}(\mathrm{t})$ is the pump light intensity, β is the monomolecular recombination constant and γ is the bimolecular recombination constant. In the case of monomolecular recombination the lifetime τ is related to the recombination constant in the following manner: $= \frac{1}{\beta}$. In the case of bimolecular recombination, $\tau = \frac{1}{\sqrt{\mathrm{g}\gamma\mathrm{I}}}$ is a good approximation for the steady state case.[6]

The solutions to the differential equation for the monomolecular case (2.4) can be found analytically to be

$$N(t) = \frac{gI_o\tau}{2}\left[1-\frac{2+(\omega\tau)^2}{1+(\omega\tau)^2}e^{-t/\tau}\right] + \frac{gI_o\tau}{2[1+(\omega\tau)^2]}(\omega\tau\sin\omega\tau + \cos\omega\tau) \tag{2.6}$$

where ω, the pump modulation frequency, appears in the solution because it is part of $I_L(t)$. When the sample is initially illuminated the portion of the solution with the exponential term dominates, however in steady-state conditions (which is where I make PIA measurements) the exponential term becomes negligible and it is evident for the case of monomolecular recombination that $N(t)$ depends linearly on the pump intensity I_o. Furthermore, equation 2.6 looks like an oscillating function with an amplitude of

$$N_s = \frac{gI_o\tau}{\sqrt{1+(\omega\tau)^2}} \tag{2.7}$$

where N_s represents the amplitude of the $N(t)$ oscillation and $gI_o\tau$ is the equilibrium population N_o created by constant pump light illumination. In practice, a PIA signal—a change in transmission scaled to the total transmission—is a measurement of the amplitude of the excited state population N_s scaled to N_o. Thus for the case of purely monomolecular recombination, theory provides the following predicted relationship between the measured signal and the pump modulation frequency ω

$$\frac{dT}{T} = \frac{1}{\sqrt{1+(\omega\tau)^2}} \tag{2.8}$$

Consequently, by solving the differential equation describing monomolecular recombination (2.4) we can predict how a PIA measurement depends both on light intensity and pump modulation.

The case for bimolecular recombination (equation 2.5) can be solved analytically and as before, looks like a function that oscillates in time.[7]

$$N_s = \frac{\sqrt{\frac{gI_o}{\gamma}}\frac{\pi}{\omega\tau}\tanh\left(\frac{\pi}{\omega\tau}\right)}{\frac{\pi}{\omega\tau}+\tanh\left(\frac{\pi}{\omega\tau}\right)} \tag{2.10}$$

In steady-state conditions when $\omega\tau \ll 1$ the PIA signal is independent of ω and the following relationship is found for intensity:

$$N_s = \sqrt{\frac{gI_o}{\gamma}} \tag{2.9}$$

thus

$$\frac{dT}{T} \propto \sqrt{I_o} \tag{2.11}$$

To reiterate, as we consider how PIA signal varies depending on the pump light intensity I_o, we would expect from the theory to measure a linear dependence for the case of pure monomolecular recombination and in the case of purely bimolecular recombination we would expect to find a power law dependence that has a power of ½. Consequently, for a real system with both processes simultaneously occurring we would expect to see a power law dependence with a power that lies between 0.5 and 1. Or more explicitly, we fit the data to

$$\frac{dT}{T} \propto (I_o)^b \qquad \text{where } 0.5 < b < 1 \qquad (2.12)$$

In turn, in considering how PIA signal depends on the frequency of pump modulation ω, we would expect from the theory to see no dependence in the case of bimolecular recombination and in the case of monomolecular recombination, we would expect to be able to fit the data to equation 2.8 to determine a value for the lifetime τ. In practice, however, the relationship between PIA signal and ω is more complex than the simple cases of pure monomolecular and pure bimolecular recombination. Here I quote directly from Wohlgenannt et al.

> Since films of conjugated polymer, in general, are very inhomogeneous at the molecular level, they resemble amorphous materials. They dynamics of photoexcitations in amorphous materials is governed in many cases by a "dispersive" process. In a dispersive process, the response, $N(\omega)$, of the system to a modulated excitation depends non-trivially on a fractional power of the (modulation) frequency ω. […]The dispersive response […] is phenomenological in the sense that [the models were] not derived from a rate equation, but rather [were] invoked in order to account for the [experimental observation]. (pg 213, 215)

There are three (related) dispersive models used to fit frequency dependent data referred to as the Cole-Cole,[8, 9] the Davidson-Cole[10] and the Havriliak-Negami[11] models. These models were developed to fit the complex dielectric constant and were developed by considering the curvature/shape of plotting the imaginary vs the real component of the dielectric constant. As applied to modulation dependent PIA data, the models go as follows:

$$\frac{dT}{T} = \frac{1}{1 + (i\omega\tau)^{\alpha}} \qquad \text{Cole-Cole} \qquad (2.13)$$

$$\frac{dT}{T} = \frac{1}{(1 + i\omega\tau)^{\beta}} \qquad \text{Cole-Davidson} \qquad (2.14)$$

$$\frac{dT}{T} = \frac{1}{(1 + (i\omega\tau)^{\alpha})^{\beta}} \qquad \text{Havriliak-Negami} \qquad (2.15)$$

In all three models, the devil lies in taking i to a power. Wohlgenannt et al. tackle this issue for the Cole-Cole model (equation 2.13) by finding the real (or in-phase (I)) component and the imaginary (or quadrature (Q)) component for this model to be

$$\left(\frac{dT}{T}\right)_I = \frac{1 + (\omega\tau)^{\alpha}\cos(\pi\alpha/2)}{1 + 2(\omega\tau)^{\alpha}\cos(\pi\alpha/2) + (\omega\tau)^{2\alpha}} \qquad (2.15)$$

and

$$\left(\frac{dT}{T}\right)_Q = \frac{(\omega\tau)^\alpha \sin(\pi\alpha/2)}{1 + 2(\omega\tau)^\alpha \cos(\pi\alpha/2) + (\omega\tau)^{2\alpha}} \tag{2.16}$$

From this we appreciate that both the in-phase and quadrature signals are valuable and can contribute to how we understand the relationship between PIA signal and modulation frequency ω in a real blend where both monomolecular and bimolecular recombination processes occur.

To conclude this section, I want to acknowledge the fact that significant knowledge can made available through PIA data. Specifically, the theoretical foundation of PIA indicates how we are able to use this technique to access information about lifetime and recombination dynamics.

Chapter 2 Conclusion

In this chapter I have discussed details of the experiments I have done to characterize my solar cell devices and material systems. EQE spectra, IV curves, PLE spectra and PIA data all worked to inform my understanding of device response and functionality in a variety of polymer/QD blends. As evidenced in the other chapters of this dissertation, each technique helped to unveil part of the device physics occurring as the system responds to light.

Figures for Chapter 2

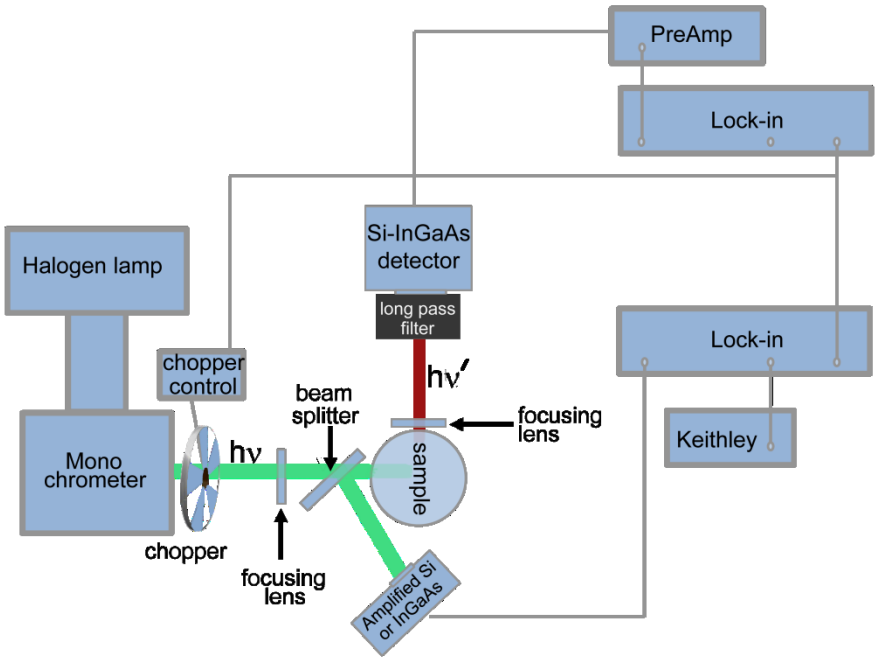

Figure 2 schematic of the PLE set up

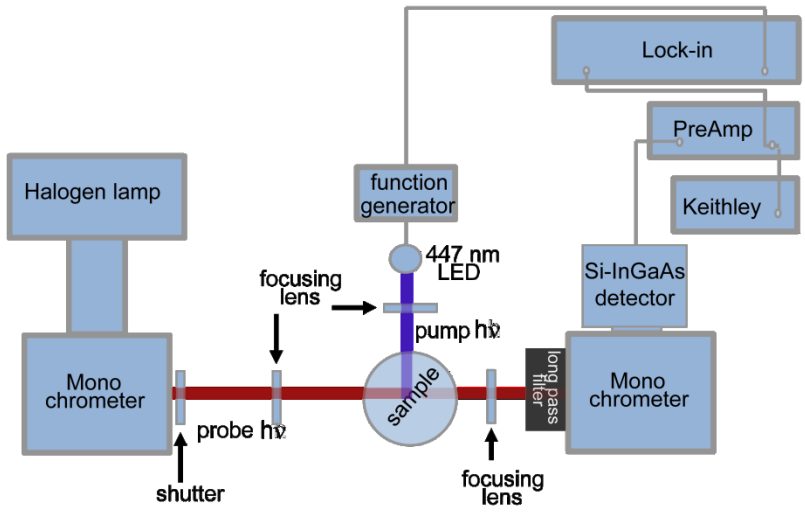

Figure 3 schematic of the PIA set up

1. V. Shrotriya, G. Li, Y. Yao, T. Moriarty, K. Emery and Y. Yang, *Advanced Functional Materials*, 2006, **16**, 2016-2023.
2. K. Emery, in *Handbook of Photovoltaic Science and Engineering*, eds. A. Luque and S. Hegedus, John Wiley & Sons, 2nd edn., 2011, ch. 18, pp. 797-840.
3. M. Pope and C. E. Swenberg, *Electronic Processes in Organic Crystals and Polymers*, Oxford University Press, New York, 1999.
4. D. S. Ginger and N. C. Greenham, *Physical Review B*, 1999, **59**, 10622-10629.
5. M. Wohlgenannt, E. Ehrenfreund and Z. V. Vardeny, in *Photophysics of Molecular Materials: From Single Molecules to Single Crystals*, ed. G. Lanzani, Wiley-VCH, Weinheim, 2006, ch. 5, pp. 183-259.
6. C. Botta, S. Luzzati, R. Tubino, D. D. C. Bradley and R. H. Friend, *Physical Review B*, 1993, **48**, 14809-14817.
7. G. Dellepiane, C. Cuniberti, D. Comoretto, G. F. Musso, G. Figari, A. Piaggi and A. Borghesi, *Physical Review B*, 1993, **48**, 7850-7856.
8. K. S. Cole and R. H. Cole, *Journal of Chemical Physics*, 1941, **9**, 341-351.
9. K. S. Cole and R. H. Cole, *Journal of Chemical Physics*, 1942, **10**, 98-105.
10. D. W. Davidson and R. H. Cole, *Journal of Chemical Physics*, 1951, **19**, 1484-1490.
11. Havrilia.S and S. Negami, *Polymer*, 1969, **10**, 859-&.

Chapter 3: Charge Generation and Energy Transfer in Hybrid Polymer/Infrared Quantum Dot Solar Cells

original article can be found at http://pubs.rsc.org/en/content/articlelanding/2013/ee/c2ee24175g

1. Introduction

The last decade has seen dramatic progress in the use of solution-processed lead chalcogenide quantum dots as IR light harvesters in both imaging sensors and solar cells.[1-4] As the power conversion efficiency of IR band gap colloidal quantum dot solar cells has climbed from under 1%[5, 6] to over 7%,[7] the field has also demonstrated impressive scientific achievements such as the observation of hot electron transfer,[8] and the demonstration of internal quantum efficiencies over 100% in photovoltaic mode.[9, 10] These advances have been achieved through improvements in quantum dot surface chemistry,[11-14] control of doping levels,[15-18] and improved device architecture,[19] often by utilizing interlayers[20-23] and other strategies commonly used with organic photovoltaic devices.

While the majority of recent PbS and PbSe quantum dot-based device studies have focused on inorganic heterojunction concepts,[3, 9, 23, 24] hybrid heterojunctions between organic semiconductors and lead chalcogenide quantum dots are of significant interest,[25-30] both from a processing/mechanical stability standpoint, and because of the possibilities to rapidly extract carriers from excited dots at a heterointerface,[31] or to harness novel physics—like singlet fission[10]—occurring in the organic component. The range of hybrid organic/inorganic architectures of interest includes planar donor/acceptor heterojunctions,[10] ternary donor/acceptor/acceptor bulk heterojunction blends,[29, 32-34] and binary donor acceptor blends.[26-28, 30, 35-37] These combinations exhibit the possibility for a rich range of photophysics, including various combinations of charge and energy transfer, and a range of different pathways could result in the generation of photocurrent.

Early binary bulk heterojunction devices made with IR-band gap quantum dots such as PbSe or PbS and widely used conjugated polymers such as polythiophenes or poly-*p*-phenylene-vinylene derivatives as host matrices exhibited disappointingly low performance compared with blends made with CdSe quantum dots.[25] However, we recently showed that the use of new host polymers can support long-lived (microsecond and longer) photo-induced charge transfer,[27] and that blends exhibiting characteristic long-lived photoinduced charge separation at the organic/PbS interface can exhibit dramatic (~100X) improvements in photocurrent compared to blends that do not.[26, 27]

Herein, we seek to understand photocurrent generation mechanisms in conjugated polymer/PbS blends in more detail by comparing the spectroscopic properties and photovoltaic behavior of blends of PbS quantum dots with three recently developed organic semiconductor hosts, including the newly reported conjugated polymers poly[(4,4’-bis(3-(2-hexyl-decyl)dithieno[3,2-b:2’,3’-d]pyrrole)-2,6-diyl-alt-(2,5-bis(3-(2-ethyl-hexyl)thiophen-2yl)thiazolo[5,4-d]thiazole)] PPEHTT, and poly[(4,4'-bis(2-octyl)dithieno[3,2-b:',3'-d]silole)-2,6-diyl-alt-(2,5-bis(3-octylthiophen-2yl)thiazolo[5,4-d]thiazole)] (PSOTT[38, 39]) with the previously reported bulk heterojunction blend PDTPQx-HD.[26] We find that PDTPQx-HD and PPEHTT

quantum dot blends both exhibit signatures consistent with classic polymer/quantum dot bulk heterojunctions,[26, 27, 40, 41] including long-lived photoinduced charge transfer. On the other hand, the operating mechanism of PSOTT/PbS blends seems different. We hypothesize this blend may operate as a Schottky diode sensitized by energy transfer from the polymer host. Such a mode could open new possibilities for engineering device structures for light harvesting in low bandgap quantum dot solar cells.

2. Experimental Methods

2.1 Synthesis of polymers

The synthesis of PDTPQx-HD[27] and PSOTT[38, 39] are described elsewhere. PPEHTT was synthesized from 2,5-Bis-[5-bromo-(2-ethyl-hexyl)-thiophen-2yl]-thiazolo[5,4-d]thiazole[38] and 2,6-Di(trimethyltin)-*N*-(1-hexyldecyl)dithieno[3,2-*b*:30-*d*]pyrrole[42] by Stille polycondensation reaction. Details are given in Appendix 1. PDTPQx-HD, PPEHTT and PSOTT had number average molecular weights (M_n) of 8.1, 8.4 and 10.8 kDa and a polydispersity index (PDI) of 1.6, 1.6 and 3.3, respectively, as determined by performing gel permeation chromatography (GPC) relative to polystyrene standards in chlorobenzene at 60 °C.

2.2 Synthesis of PbS quantum dots

PbS quantum dots were synthesized, extracted and washed following the route of Hines *et al.*[43] and modified as previously reported.[26] To vary the quantum dot size the injection temperature and reaction time were varied as needed. The largest quantum dots (band gap = 0.7 eV) had precursor injected at 165°C and grown for one hour. The smallest quantum dots (band gap = 1.6 eV) had precursor injected at 100°C and the reaction was immediately immersed into an ice bath. All other synthesis fell within these two bounds (for example, an injection at 140°C and growth for 2 min yielded dots with a band gap of ~1.25 eV). Prior to blending the quantum dots with the polymers, the oleic acid ligands passivating the as-synthesized PbS quantum dots were exchanged for butylamine as described elsewhere.[26] Quantum dot synthesis and ligand exchange were performed using standard air free techniques outside of the glove box. The quantum dots were then suspended in either anhydrous chlorobenzene or anhydrous dichlorobenzene (Sigma Aldrich) at high concentrations between 150-450 mg/mL. Typically, quantum dots were synthesized, ligand-exchanged, and incorporated into devices within 24 hours of synthesis. All solution processing was done in the glove box.

2.3 Device Fabrication and Testing

Pre-etched ITO substrates were initially cleaned by sonicating in acetone and isopropyl alcohol, followed by air-plasma cleaning for 5 min in a Harrick Plasma Cleaner PDC-32G, 18W applied. We then spin coated 40 nm of PEDOT:PSS (Baytron® P VP Al 4083, filtered with 0.45 µm PVDF filter) onto the ITO. The PEDOT layer was then annealed under nitrogen flow for 15-20 min at 120 °C. All subsequent fabrication steps took place in the glovebox. First, the active area solution was spin-coated and the resulting film was thiol treated by drop-casting a solution of 100 mM ethanedithiol in acetonitrile onto the surface and then wicking the drop away. Electrical contacts of LiF (0.7 nm) and Al (65 nm) were deposited by thermal evaporation at a base pressure of less than 1 X 10^{-6} torr. The PDTPQx-HD and PPEHTT solutions were prepared at 25 mg/mL w/v using anhydrous chlorobenzene (Sigma Aldrich) as the solvent and heated to 45°C. The polymer solution was typically prepared 24 hours prior to use. The solutions were always filtered immediately prior to use with a 0.2µm filter. PDTPQx-HD and PPEHTT polymer/quantum dot blend solutions were spin coated at room temperature.

PSOTT solutions were prepared at a concentration of 6 mg /mL w/v in dichlorobenzene and heated to 130°C for at least one hour before use. PSOTT and quantum dot solutions were filtered separately prior to mixing, and the blended solution was returned to heat at 120°C before spin-coating from the hot solution onto the PEDOT layer. In all cases we used a 9:1 quantum dot:polymer (w/w) loading by mixing appropriate volumes of polymer and quantum dot solution.

All external quantum efficiency (EQE) testing was carried under dynamic vacuum. Photocurrent was recorded with a Keithley 2400. Monochromated light (Acton) from a 100W tungsten halogen bulb (Oriel) provided the illumination source. EQEs were calculated using a calibrated Si-photodiode (OSI optoelectronics) for wavelengths between 400-980 nm and with a calibrated InGaAs photodiode (Thorlabs) for all wavelengths greater than 980 nm. The device pixels and the calibrated photodiode are masked to identical active areas.

2.4 Photoinduced Absorption

PIA samples were made by spin coating the active-area solution onto clean glass slides in the glovebox and treating them with ethanedithiol as described above. Standard lock-in techniques were used to obtain PIA spectra.[25, 41] Light from a filtered 447 nm light-emitting diode (LED; Luxeon Rebel, 700mA, LXML-PR01) was modulated with an Agilent 33120A waveform generator and used as an optical pump to excite the sample. Long-lived signals were monitored by a monochromated tungsten halogen lamp which served as the probe beam. A Si/InGaAs dual-band photodetector (Thorlabs, DSD2) was used to collect signal. At each energy probed, data are reported as fractional change in transmission (dT/T). The lock-in is phased to the chopper modulation so that fast absorptions appears as a negative dT/T signals in X while fast bleaches are positive in X. The reported signal was corrected for sample photoluminescence (PL) and any scattered light. All PIA measurements reported here were carried out under dynamic vacuum at room temperature.

2.5 Photoluminescence Excitation Measurements

Photoluminescence excitation (PLE) samples were made by spin coating on glass in the same way as the PIA samples. Since EDT treatment tends to quench the signal[44] we need to monitor (the quantum dot photoluminescence) the presented samples were left untreated. The same monochromated tungsten halogen lamp used for PIA spectroscopy was used as the excitation source and sample photoluminescence intensity was monitored with the same Si/InGaAs dual-band photodetector (ThorLabs, DSD2). A 900 nm long pass filter was used to filter excitation light in the pristine PSOTT spectrum, and a 1300 nm long pass filter was used to filter both scattered excitation light and polymer PL in the pristine PbS, PSOTT/PbS, and pristine PSOTT control samples. Samples were held under dynamic vacuum with the film facing the excitation light. Emitted light was wave-guided from the side of the glass substrate and focused using two aspheric lenses mounted in front of the photodetector. A fraction of the excitation light was split with a glass microscope slide to monitor the excitation intensity with an amplified silicon ($\lambda <= 1000$ nm) or an amplified InGaAs ($\lambda > 1000$ nm) photodetectors. All spectra were normalized to the excitation intensity. Spectra for Pristine PbS and PSOTT/PbS were normalized to the nanocrystal exciton peak at ~1160 nm. The pristine PSOTT spectra were scaled to match the blend intensity at 600 nm.

3. Results and Discussion

Fig. 1 shows absorption spectra for typical PbS samples as well as the chemical structures, absorption, and photoluminescence spectra for all three studied polymers. As indicated in the chemical structures, there is variation in side chain topology: PSOTT is unique because it does not include any branched side chains. Fig. 1 also includes a plot of the approximate energy levels relevant for charge separation positions for all materials as derived from a combination of cyclic voltammetry (see SI.1), optical absorption, and literature reports.[45] From these energy levels, we expect that photoinduced electron transfer should be energetically favorable from all three polymers to a wide range of PbS quantum dot sizes, making each blend a promising candidate for a hybrid bulk heterojunction device structure. Nevertheless, previous work has shown that solution-derived energy level schemes are not always successful in predicting charge transfer in solid state quantum dot/polymer blends.[25-27] This is likely because excited state redox potentials are better predictors of electron transfer in molecular systems than the ground state energy offsets,[46] and perhaps also due to differences in solvation and surface dipole effects between the solution electrochemistry and solid state film environments of the quantum dots and polymers.

We have found photoinduced absorption (PIA) spectroscopy to be a better predictor of polymer/quantum dot device performance than comparison of the energy levels via cyclic voltammetry.[26, 27] We thus performed PIA on blends of all three polymers with PbS quantum dots. We repeatedly prepared 9:1 (w/w) blends of each polymer with varying sizes of PbS quantum dots. After deposition all films were treated with ethanedithiol as described in the methods section.

Figures 2a-c shows the resulting PIA spectra recorded on PDTPQx-HD/PbS, PPEHTT/PbS, and PSOTT/PbS blend films at room temperature under vacuum. The PDTPQx-HD/PbS blend in Fig. 2a shows a broad photoinduced absorption feature below the polymer bandgap at ~1.1 eV, consistent with our previous work, and with the PIA spectra of PDTPQx-HD/fullerene blends (Appendix 1 Fig. S3). The PPEHTT/PbS blend also shows a broad photoinduced absorption in the polymer bandgap, with PIA peaks at 1.24 and 1.68 eV. Based on the similarity of these PIA features with those observed in PPEHTT/fullerene blends (Appendix 1 Fig. S3) we assign these features to positive polarons on the PPEHTT polymer. We thus conclude that both PDTPQx-HD/PbS and PPEHTT/PbS blends yield long lived charge carriers when irradiated with light.

Fig. 2c shows the PIA spectrum for a PSOTT/PbS blend at room temperature. In contrast with the other two polymers, we observe no long-lived photoinduced absorption features in the PSOTT blend. However, a reference PSOTT/ $PC_{71}BM$ blend does show a clear polaron peak at ~1.1 eV, indicating that the PSOTT polaron exhibits an absorption feature in this energy window (Appendix 1 Fig. S3). Although polymer/$PC_{\mathbf{61}}BM$ blends do exhibit a weak radical anion peak at ~1.2 eV that is typically buried under the polymer radical cation, $PC_{\mathbf{71}}BM$ radical anions exhibit a weak absorption at ~0.9 eV (again often buried under the larger polymer cation absorption).[47] We thus assign the peak at 1.1 eV in the PSOTT/ $PC_{71}BM$ to a polymer polaron. The absence of this polaron feature in the PSOTT/PbS blends when irradiated with light suggests one of two possibilities: (1) there is virtually no polaron formation within this material system or (2) polarons form but immediately undergo very fast (<< 1 μs) recombination. While these results suggest ultrafast transient absorption spectroscopy experiments could be interesting to pursue for this system, we find the second possibility less likely given that the PSOTT/fullerene blend exhibits a long lived polymer polaron feature, and that the recombination times in the polymer quantum dot blends are usually slower than recombination lifetimes in polymer/fullerene blends due to carrier trapping on the quantum dots.[27] In any case, both possibilities--a lack of polaron formation, or fast recombination--would tend to limit the efficiency in PSOTT/PbS blends.

To test the photocurrent response of these blends, we fabricated classic sandwich device structures using ITO/PEDOT:PSS bottom and LiF/Al top contacts, and the EDT treated polymer/PbS blend. (Fig. 3d). As with the PIA samples we repeatedly prepared 9:1 (w/w) blends of each polymer with varying sizes of PbS quantum dots to yield active area films of ~40-60 nm thickness.

Figures 3a-c show the resulting external quantum efficiency vs. wavelength plots for the PDTPQx/PbS, PPEHTT/PbS, and PSOTT/PbS blends, respectively. The data in Figures 3a-c show substantial photocurrents from the visible out to the near IR for all three blends.

Figures 3a-c also include absorption spectra of the respective polymer and quantum dot batches used in each device. By comparing these plots with the EQE curves in Figure 3, we conclude that all three blends show photocurrent contributions from both the quantum dot and polymer components. Indeed at the absorption onset of the polymer the EQE curves tend to show increased photocurrent, and these are particularly pronounced in the case of the PSOTT/PbS blend. The response in EQE to polymer absorption is to be expected because the quantum dot components are weaker absorbers on a per-volume basis than the conjugated polymers.

These EQE results are significant because, to our knowledge, only three polymers[26, 28, 37] have ever yielded photoresponses greater than a few percent EQE when blended with PbS quantum dots.[6] The functionality demonstrated by PSOTT and PPEHTT have thus expanded the library of polymers that give significant photoresponse in binary blends with lead chalcogenide quantum dots by two-thirds.

Perhaps more importantly, these results are intriguing because, based on our previous experiments[26] we would expect only those blends that produce long-lived polaron signatures in a PIA experiment, namely the PDTPQx-HD/PbS and PPEHTT/PbS blends, to produce substantial photocurrents. The PSOTT/PbS blend, with no detectable PIA signal, would thus be expected to be a poor performer.

In order to explain the photocurrent in the PSOTT/PbS blend, we hypothesize that it may be possible for a polymer/PbS blend to exhibit a photocurrent in the absence of a type-II heterojunction between the polymer and the quantum dots, if the quantum dots exist at sufficient loading in the film to form an effective percolation pathway between the dots and both electrodes, thereby forming a Schottky diode cell suspended in the polymer (see Appendix 1 SI.5 for a schematic diagram). This hypothesis is consistent with the fabrication differences between the current films and our earlier studies.[26] In contrast with our earlier work, the current devices were post-treated with EDT, a cross-linking dithiol that has been shown to dramatically improve the performance of PbS films in Schottky diode cells (indeed, without the EDT treatment, PSOTT/PbS devices show negligible photocurrent, see Appendix 1 SI.6).

However, while this Schottky-diode-within-a-blend picture is consistent with the modest photocurrents observed in the IR portion of the spectrum, it cannot by itself account for the dramatic increase in EQE we observe at the polymer absorption edge. We thus speculate that the polymer may also be acting as an energy funnel by undergoing rapid energy transfer to the quantum dots (for a visual representation of this process see SI.5). Such a circumstance would explain both the PIA data and the device photocurrent for the PSOTT/PbS device. The EQE spectrum unequivocally demonstrates polymer participation in photocurrent generation--energy transfer events from the polymer to the quantum dot would certainly promote the circumstance of increased photocurrent generation as the polymer starts absorbing light. Energy transfer would also explain the lack of long-lived signal in the PIA spectrum: while PIA is a powerful tool for detecting charge transfer, it is blind to the occurrence of energy transfer events.

To test the plausibility of this energy transfer hypothesis, we collected photoluminescence excitation (PLE) spectra by monitoring the quantum dot photoluminescence signal while sweeping the excitation light on the following three different films: pristine PSOTT, neat PbS and a PSOTT/PbS blend. Figure 4 shows the resulting PLE data. As expected, the PLE trace for the pristine quantum dot film (detected at the quantum dot emission peak (dashed green line) tracks the quantum dot absorption spectrum. Likewise the neat PSOTT polymer film shows no detectable emission at the quantum dot emission peak (thin gray line), and a PLE trace that follows the polymer absorption spectrum when detected at the polymer emission peak (dotted blue line). Notably, the PLE trace for the PSOTT/PbS quantum dot blend (collected at the *quantum dot emission*) shows a strong feature that exactly matches the polymer absorption peak, providing strong evidence that energy transfer can indeed occur from PSOTT to PbS quantum dots in this size range.

While it seems clear from the PIA experiments that the three polymers studied, PDTPQx-HD, PPEHTT, and PSOTT behave differently, we note that there are several differences – both energetic and structural -- between the PSOTT polymer and the other two that might play a role in their different behaviors when blended with PbS quantum dots. We note that side-chain branching has been shown to influence organic solar cell device performance,[38, 48] and PSOTT possess linear side chains, while the PDTPQx-HD and PPEHTT polymers possess branched side chains. Additionally, the PSOTT used in these studies had both a higher average average molecular weight and polydispersity relative to the other two polymers. Finally, the differences in the balance of charge and energy transfer could result from variations in the different polymer energy levels as they align with the quantum dot energy levels. We note that of the three studied polymers, the measured ground state ionization energy of PSOTT (-5.09 eV) is roughly isoenergetic with that of the PbS quantum dots. These factors, alone or in combination, could all be expected to impact charge transfer in these blends.

Conclusion

From a scientific and technical standpoint, hybrid heterojunctions offer the potential to combine the best of both organic and inorganic materials, including chemical tailorability of energy gaps and interfacial states, single-step solution processing, mechanical flexibility, and long-term stability. These properties would be extremely advantageous for efficient single and tandem solar energy harvesting devices. Here, we have compared the photophysical and device properties of several different polymer/IR quantum dot blends. Importantly, we have shown that it is possible to fabricate a hybrid thin film device that exhibits strong photocurrent contribution from absorption on both the polymer and quantum dot components, but does not exhibit the typical spectral signature of large populations of long-lived (microsecond-millisecond) photoinduced charge residing on the polymer. Since photoluminescence excitation data show that strong energy transfer occurs from the polymer to the PbS quantum dots in this blend we thus propose that these devices may be operating as energy-transfer-sensitized quantum-dot Schottky diodes. If such behavior can be realized with other organic sensitizers, it might be possible to adopt an energy-relay strategy[49,50] to sensitize quantum dot solar cells for improved light harvesting, especially just blue of the excitonic peak, where most inorganic quantum dot solar cells presently exhibit a marked dip in their spectral response.

Acknowledgements

This work was supported by the U.S. Department of Energy, Office of Basic Energy Sciences, Division of Material Sciences, under Award DE-FG02-07ER46467. C.WS. acknowledges partial support from the NSF SEES fellowship program (GEO-1215753). The authors wish to acknowledge the Nanotechnology User Facility for the use of the TEM and Keiko Munechika for imaging the PbS quantum dots included in fig. 1.

Notes and References

see Appendix 1 for further details: [includes PPEHTT synthesis, cyclic voltammograms of the three polymers, photoinduced spectroscopy measurements on (1)neat quantum dots, (2)polymer/fullerene blends, and (3)PSOTT/quantum dot blend compared against a sample of clean PSOTT, a schematic diagram of PSOTT/PbS schottkey diode, EQE data from a PSOTT/PbS device that did not undergo post-film ligand exchange, and light IV curves for all devices reported in the paper].

Figures for Chapter 3

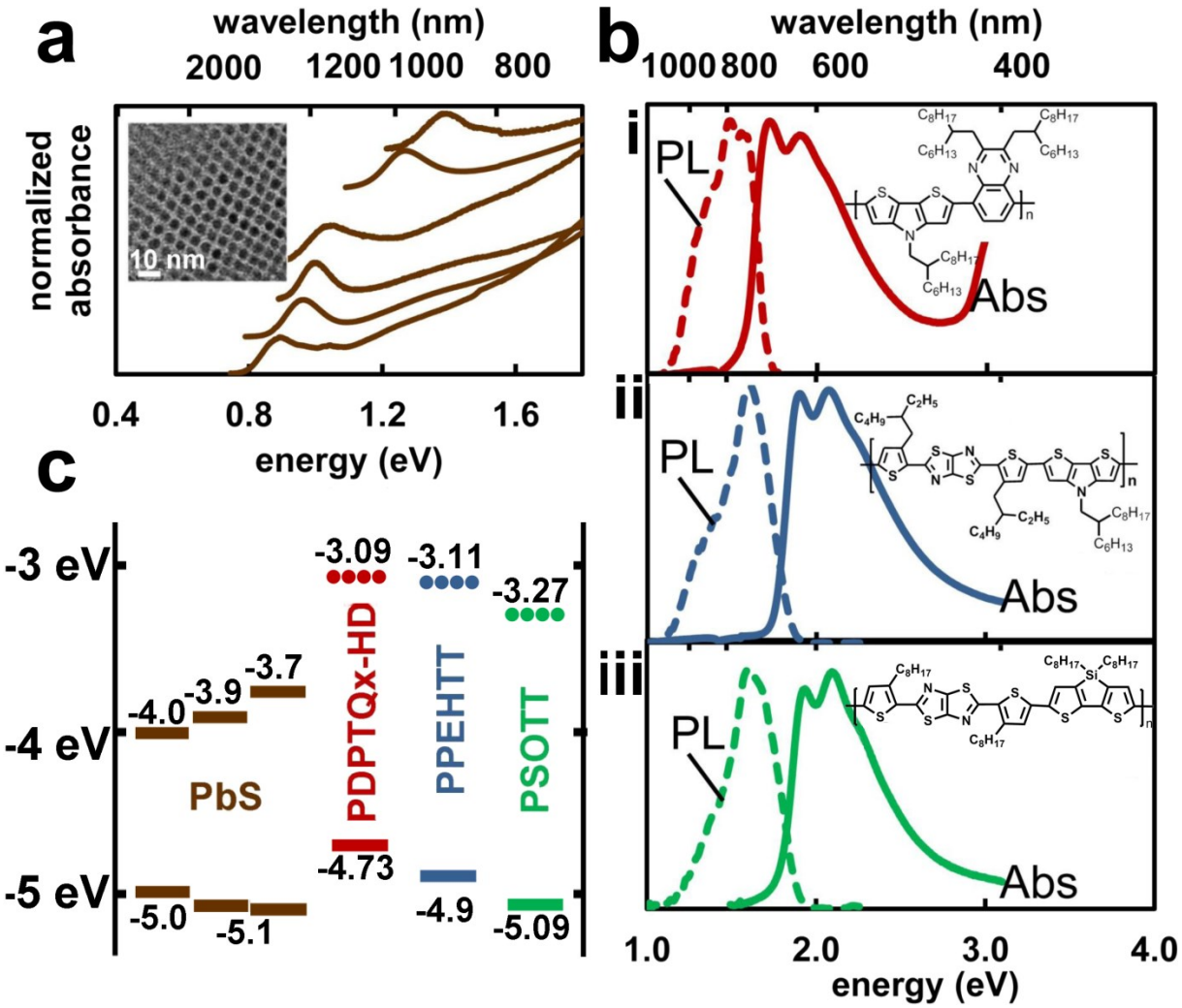

Figure 1

Absorption, photoluminescence and energy levels characterizing the donor and acceptor materials. Figure 1a shows absorption spectra for the PbS quantum dots with a TEM image of a typical batch in the inset. In this work, features associated with the quantum dots shift in energy depending on the size of the quantum dots used in for a given polymer/quantum dot sample. Figure 1bi-iii shows the photoluminescence (dashed lines), absorption(solid lines) and chemical structures of the polymers studied, PDTPQx-HD, PPEHTT and PSOTT respectively. Figure 1c gives energy level values for the quantum dots and polymers. Note: more quantum dot batches were synthesized than are included in the figure. Energy levels for the PbS quantum dots are taken from literature tabulated from the convention of Hyun et al. in which the LUMO is determined from CV data on oleic acid capped PbS quantum dots with a Ag/AgCl reference in NaCl that is assumed 4.7 eV below vacuum and the HOMO is calculated by subtracting the band gap measured for the quantum dots. No corrections were made due to the exciton binding energy.[45] Ground state ionization energy levels for the polymers are as

determined by cyclic voltammetry with a SCE reference that is assumed 4.4 eV below vacuum (see SI.1). The excited state ionization energy (dashed lines) was assigned using the optical bandgap determined from the intersection point of the photoluminescence and absorption traces.

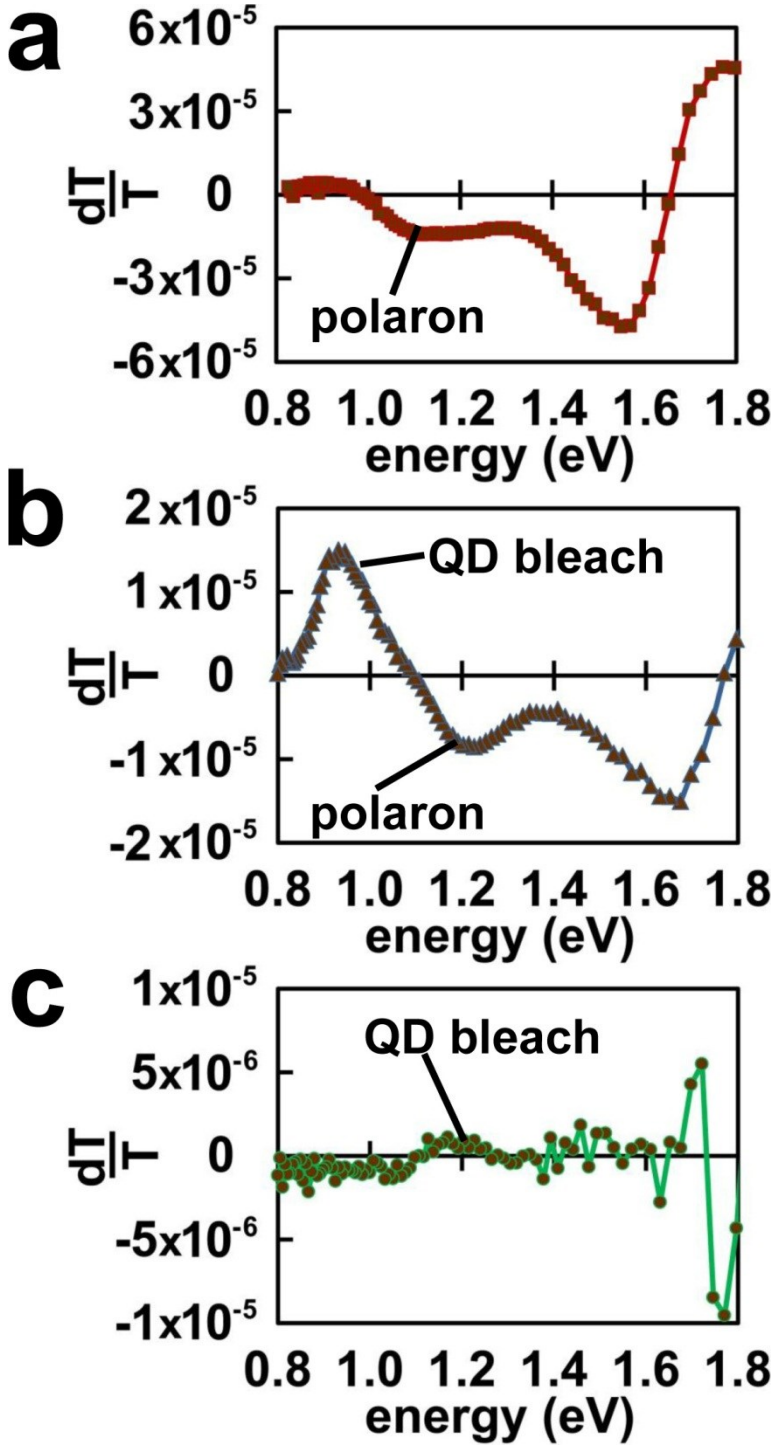

Figure 2 In-phase signal from photoinduced absorption (PIA) for quantum dot/polymer blends. 2a is blended with PDTPQx-HD, 2b is with PPEHTT and 2c is with PSOTT. Absorption at the pump

frequency for these samples was 0.589, 0.587, and 0.258 respectively. It should be noted that in earlier studies we found significant polaron signal (>60ppm) for the PDTPQx-HD/PbS blend with an absorption of 0.273 at the pump frequency. [27] Also of note, the quantum dot bleach feature is not observed in 2a because smaller sized dots were used and the bleach feature does not out-compete the polaron absorption feature. The polaron feature is absent in 2c, the PSOTT/PbS blend, suggesting that upon excitation no significant charge transfer takes place between this polymer and the quantum dot.

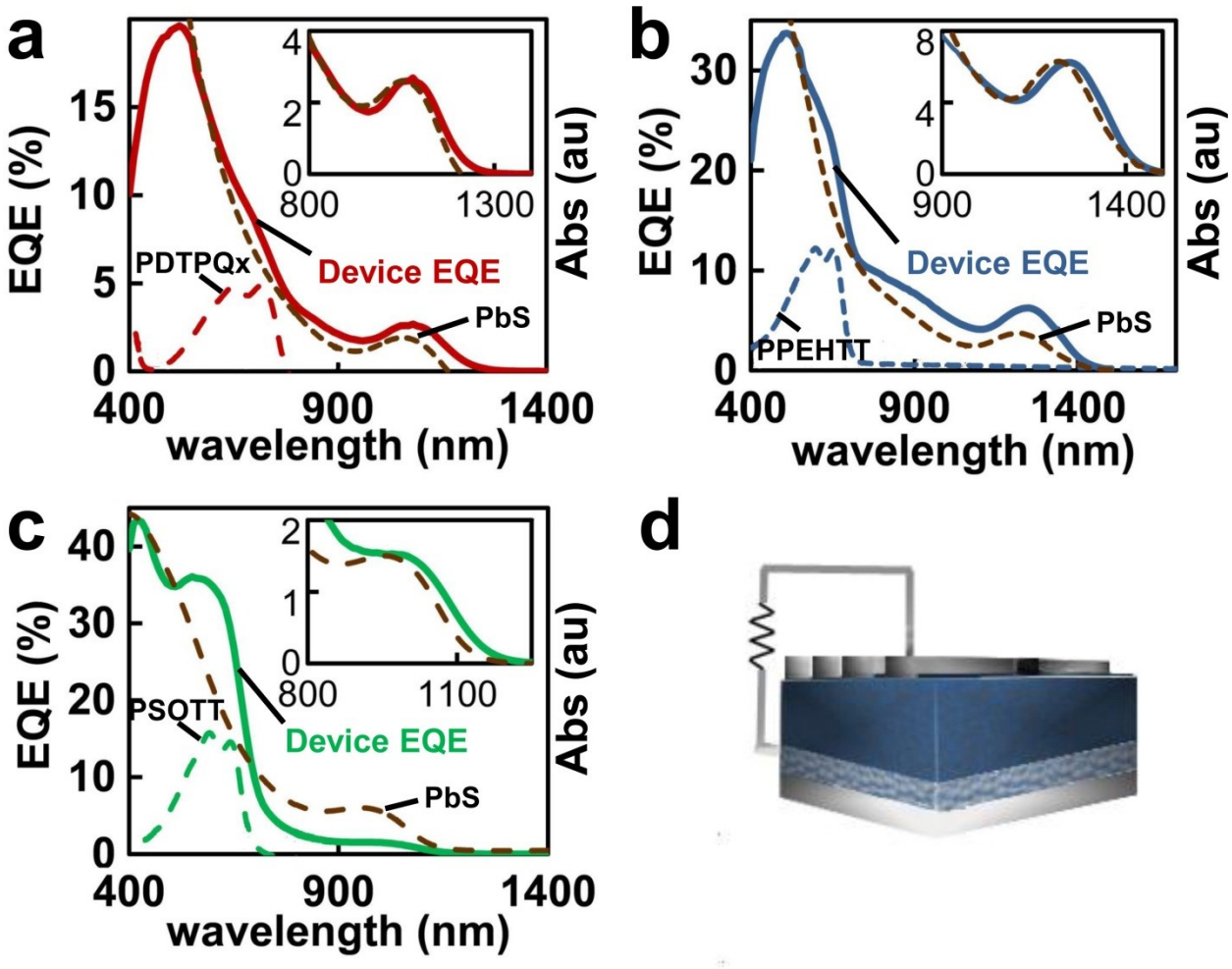

Figure 3a-c EQE device data (solid line) overlayed with absorption data (dashed lines) for the component materials used in each respective device. The active layer is PDTPQx-HD/PbS in 3a, PPEHTT/PbS in 3b, and PSOTT/PbS in 3c. The IR portion of the EQE data are highlighted in the inset with the quantum dot absorption scaled to the peak in the EQE data. (Axes titles for the insets are not shown but follow the titles for the full spectrum data.) Note that in all cases the increase in EQE shoulder maps to the absorption of the respective polymer. The effect is particularly pronounced for the PSOTT/PbS system. **3d** shows the device architecture for all the devices ITO-coated glass as one contact, 40 nm of PEDOT:PSS, 40-60 nm of active area, 0.7 nm LiF and 65 nm Al for the other contact. As pictured, the sample is illuminated from the bottom. (Note: not drawn to scale.)

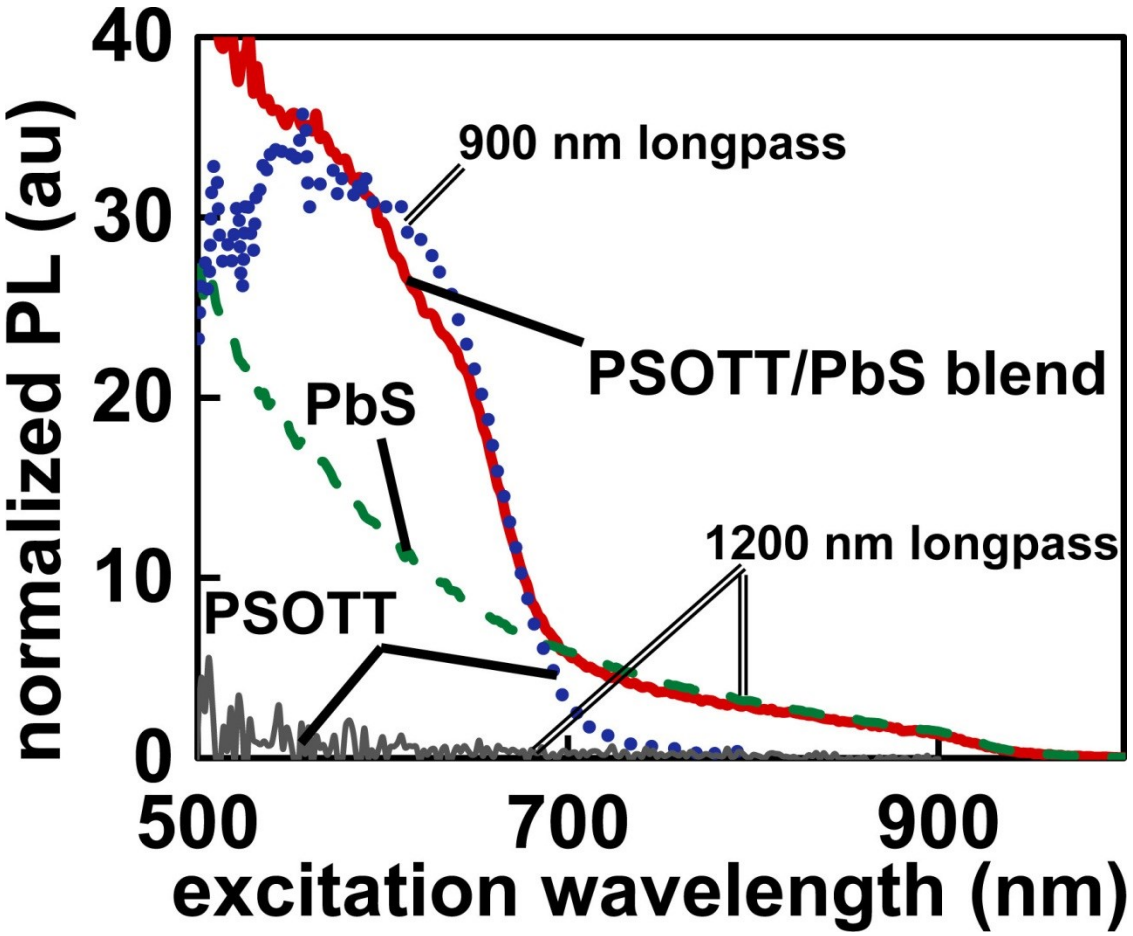

Figure 4 Photoluminescence excitation data. The red (solid) line is signal from light detected at wavelengths greater than 1200 nm for PSOTT blended with PbS. The blue (dotted) line is signal from light detected at wavelengths greater than 900 for a pristine PSOTT. The green (dashed) line is signal from light from neat PbS detected at wavelengths greater than 1200 nm. The gray (thin solid) line shows that no signal is detected from pristine PSOTT at wavelengths greater than 1200 nm.

1. K. M. Noone and D. S. Ginger, *ACS Nano*, 2009, **3**, 261-265.
2. G. Konstantatos and E. H. Sargent, *Nature Nanotechnology*, 2010, **5**, 391-400.
3. E. H. Sargent, *Nature Photonics*, 2012, **6**, 133-135.
4. E. H. Sargent, *Nature Photonics*, 2009, **3**, 325-331.
5. S. A. McDonald, P. W. Cyr, L. Levina and E. H. Sargent, *Applied Physics Letters*, 2004, **85**, 2089-2091.
6. H. Fu and S. W. Tsang, *Nanoscale*, 2012, **4**, 2187-2201.
7. A. H. Ip, S. M. Thon, S. Hoogland, O. Voznyy, D. Zhitomirsky, R. Debnath, L. Levina, L. R. Rollny, G. H. Carey, A. Fischer, K. W. Kemp, I. J. Kramer, Z. Ning, A. J. Labelle, K. W. Chou, A. Amassian and E. H. Sargent, *Nature Nanotechnology*, 2012, **7**, 577-582.
8. W. A. Tisdale, K. J. Williams, B. A. Timp, D. J. Norris, E. S. Aydil and X. Y. Zhu, *Science (Washington, DC, United States)*, 2010, **328**, 1543-1547.

9. O. E. Semonin, J. M. Luther, S. Choi, H.-Y. Chen, J. Gao, A. J. Nozik and M. C. Beard, *Science (Washington, DC, United States)*, 2011, **334**, 1530-1533.
10. B. Ehrler, M. W. B. Wilson, A. Rao, R. H. Friend and N. C. Greenham, *Nano Lett.*, 2012, **12**, 1053-1057.
11. D. V. Talapin and C. B. Murray, *Science (Washington, DC, United States)*, 2005, **310**, 86-89.
12. J. M. Luther, M. Law, Q. Song, C. L. Perkins, M. C. Beard and A. J. Nozik, *ACS Nano*, 2008, **2**, 271-280.
13. K. S. Jeong, J. Tang, H. Liu, J. Kim, A. W. Schaefer, K. Kemp, L. Levina, X. Wang, S. Hoogland, R. Debnath, L. Brzozowski, E. H. Sargent and J. B. Asbury, *ACS Nano*, 2012, **6**, 89-99.
14. E. J. D. Klem, D. D. MacNeil, P. W. Cyr, L. Levina and E. H. Sargent, *Applied Physics Letters*, 2007, **90**, 183113/1-183113/3.
15. O. Voznyy, D. Zhitomirsky, P. Stadler, Z. Ning, S. Hoogland and E. H. Sargent, *ACS Nano*, 2012, **6**, 8448-8455.
16. M. Shim and P. Guyot-Sionnest, *Nature (London)*, 2000, **407**, 981-983.
17. D. Mocatta, G. Cohen, J. Schattner, O. Millo, E. Rabani and U. Banin, *Science (Washington, DC, United States)*, 2011, **332**, 77-81.
18. H. Liu, D. Zhitomirsky, S. Hoogland, J. Tang, I. J. Kramer, Z. Ning and E. H. Sargent, *Applied Physics Letters*, 2012, **101**, 151112/1-151112/3.
19. I. J. Kramer and E. H. Sargent, *ACS Nano*, 2011, **5**, 8506-8514.
20. P. R. Brown, R. R. Lunt, N. Zhao, T. P. Osedach, D. D. Wanger, L.-Y. Chang, M. G. Bawendi and V. Bulovic, *Nano Lett.*, 2011, **11**, 2955-2961.
21. E. J. D. Klem, C. W. Gregory, G. B. Cunningham, S. Hall, D. S. Temple and J. S. Lewis, *Applied Physics Letters*, 2012, **100**, 173109/1-173109/4.
22. N. Li, B. E. Lassiter, R. R. Lunt, G. Wei and S. R. Forrest, *Applied Physics Letters*, 2009, **94**, 023307/1-023307/3.
23. R. Brown Patrick, R. Lunt Richard, N. Zhao, P. Osedach Timothy, D. Wanger Darcy, L.-Y. Chang, M. G. Bawendi and V. Bulovic, *Nano Lett.*, 2011, **11**, 2955-2961.
24. A. G. Pattantyus-Abraham, I. J. Kramer, A. R. Barkhouse, X. Wang, G. Konstantatos, R. Debnath, L. Levina, I. Raabe, M. K. Nazeeruddin, M. Gratzel and E. H. Sargent, *ACS Nano*, 2010, **4**, 3374-3380.
25. K. M. Noone, N. C. Anderson, N. E. Horwitz, A. M. Munro, A. P. Kulkarni and D. S. Ginger, *ACS Nano*, 2009, **3**, 1345-1352.
26. K. M. Noone, E. Strein, N. C. Anderson, P. T. Wu, S. A. Jenekhe and D. S. Ginger, *Nano Lett.*, 2010, **10**, 2635-2639.
27. K. M. Noone, S. Subramaniyan, Q. Zhang, G. Cao, S. A. Jenekhe and D. S. Ginger, *Journal of Physical Chemistry C*, 2011, **115**, 24403-24410.
28. J. Seo, M. J. Cho, D. Lee, A. N. Cartwright and P. N. Prasad, *Advanced Materials (Weinheim, Germany)*, 2011, **23**, 3984-3988.
29. D. Jarzab, K. Szendrei, M. Yarema, S. Pichler, W. Heiss and M. A. Loi, *Advanced Functional Materials*, 2011, **21**, 1988-1992.
30. K. Szendrei, F. Cordella, M. V. Kovalenko, M. Boberl, G. Hesser, M. Yarema, D. Jarzab, O. V. Mikhnenko, A. Gocalinska, M. Saba, F. Quochi, A. Mura, G. Bongiovanni, P. W. M. Blom, W. Heiss and M. A. Loi, *Advanced Materials*, 2009, **21**, 683-687.
31. R. D. Schaller, M. Sykora, S. Jeong and V. I. Klimov, *Journal of Physical Chemistry B*, 2006, **110**, 25332-25338.
32. T. Rauch, M. Boberl, S. F. Tedde, J. Furst, M. V. Kovalenko, G. Hesser, U. Lemmer, W. Heiss and O. Hayden, *Nature Photonics*, 2009, **3**, 332-336.

33. G. Itskos, A. Othonos, T. Rauch, S. F. Tedde, O. Hayden, M. V. Kovalenko, W. Heiss and S. A. Choulis, *Advanced Energy Materials*, 2011, **1**, 802-812.
34. S. ten Cate, J. M. Schins and L. D. A. Siebbeles, *ACS Nano*, 2012, **6**, 8983-8988.
35. S. Dayal, N. Kopidakis, D. C. Olson, D. S. Ginley and G. Rumbles, *Nano Lett.*, 2010, **10**, 239-242.
36. S. Dayal, M. O. Reese, A. J. Ferguson, D. S. Ginley, G. Rumbles and N. Kopidakis, *Advanced Functional Materials*, 2010, **20**, 2629-2635.
37. C. Piliego, M. Manca, R. Kroon, M. Yarema, K. Szendrei, M. R. Andersson, W. Heiss and M. A. Loi, *Journal of Materials Chemistry*, 2012, **22**, 24411-24416.
38. S. Subramaniyan, H. Xin, F. S. Kim, S. Shoaee, J. R. Durrant and S. A. Jenekhe, *Advanced Energy Materials*, 2011, **1**, 854-860.
39. H. Xin, S. Subramaniyan, T.-W. Kwon, S. Shoaee, J. R. Durrant and S. A. Jenekhe, *Chemistry of Materials*, 2012, **24**, 1995-2001.
40. D. S. Ginger and N. C. Greenham, *Synthetic Metals*, 1999, **101**, 425-428.
41. D. S. Ginger and N. C. Greenham, *Physical Review B*, 1999, **59**, 10622-10629.
42. E. Ahmed, S. Subramaniyan, F. S. Kim, H. Xin and S. A. Jenekhe, *Macromolecules (Washington, DC, United States)*, 2011, **44**, 7207-7219.
43. M. A. Hines and G. D. Scholes, *Advanced Materials*, 2003, **15**, 1844-1849.
44. C. A. Nelson and X. Y. Zhu, *Journal of the American Chemical Society*, 2012, **134**, 7592-7595.
45. B.-R. Hyun, Y.-W. Zhong, A. C. Bartnik, L. Sun, H. D. Abruna, F. W. Wise, J. D. Goodreau, J. R. Matthews, T. M. Leslie and N. F. Borrelli, *ACS Nano*, 2008, **2**, 2206-2212.
46. G. Ren, C. W. Schlenker, E. Ahmed, S. Subramaniyan, S. Olthof, A. Kahn, D. S. Ginger and S. A. Jenekhe, *Advanced Functional Materials*, 2012, DOI: 10.1002/adfm.201201470.
47. A. Sperlich, M. Liedtke, J. Kern, H. Kraus, C. Deibel, S. Filippone, J. L. Delgado, N. Martin and V. Dyakonov, *Phys. Status Solidi-Rapid Res. Lett.*, 2011, **5**, 128-130.
48. J. M. Szarko, J. C. Guo, Y. Y. Liang, B. Lee, B. S. Rolczynski, J. Strzalka, T. Xu, S. Loser, T. J. Marks, L. P. Yu and L. X. Chen, *Advanced Materials*, 2010, **22**, 5468-5472.
49. E. T. Hoke, B. E. Hardin and M. D. McGehee, *Optics Express*, 2010, **18**, 3893-3904.
50. J.-H. Yum, B. E. Hardin, E. T. Hoke, E. Baranoff, S. M. Zakeeruddin, M. K. Nazeeruddin, T. Torres, M. D. McGehee and M. Gratzel, *ChemPhysChem*, 2011, **12**, 657-661.

Chapter 4: Hot hole transfer increases polaron yields in hybrid conjugated-polymer/PbS blends

Abstract

We use quasi-steady state photoinduced-absorption (PIA) to study charge generation in blends of poly(3-hexylthiophene-2,5-diyl) (P3HT) with PbS nanocrystal quantum dots as a function of excitation energy. We find that, per photon absorbed, the yield of photogenerated holes present on the conjugated polymer increases with pump energy, even at wavelengths where only the quantum dots absorb. We interpret this result as direct evidence for transfer of hot holes in these conjugated polymer/quantum dot blends. These results help understand the operation of hybrid organic/inorganic photovoltaics.

Main Article

Understanding the factors that regulate the efficiency of charge generation at donor/acceptor interfaces in excitonic solar cells is critical to improving the performance of a number of emerging solar energy technologies ranging from quantum dot[1-4] and organic photovoltaics,[5, 6] to hybrid solar cells including both polymer/quantum dot blends,[7-11] and emerging hybrid organic/perovskite devices.[12, 13] Especially in the case of cells relying on condensed phase donor/acceptor heterojunctions, the details of charge generation remains a topic of active investigation.[14-17] Nevertheless, while the overall design rules are not understood, current thinking is that factors such as wavefunction delocalization[18-20] charge transfer from non-thermalized "hot" states,[21-23] the total driving force for charge transfer (CT),[16, 24] coupling to higher lying CT states,[17, 25] interfacial dipoles,[17, 26] and local electric fields[14] can all play a role. Recent studies have shown that in various polymer/fullerene blends free carriers can be generated very quickly (sub-100 fs), and can benefit from excess energy above the band gap.[25] Similarly, in all-inorganic systems, ultra-fast (~6.4 fs) hot electron injection from PbS quantum dots to TiO_2 nanocrystals has been observed to be in competition with electron relaxation for PbS.[23, 27]

Compared to polymer/fullerene blends, much less is known about the mechanisms for charge generation in the hybrid polymer/quantum dot systems. We have previously reported that the internal quantum efficiency (IQE) increases proportionally to excitation energy in polymer/PbS hybrid solar cells.[8] More recently we reported data that could be interpreted as evidence for transfer of hot holes from photoexcited quantum dots to a conjugated polymer.[28] Although these results are suggestive, it has so far been difficult to separate different rates of quantum-dot-to-polymer hole transfer and polymer-to-quantum-dot electron transfer from the signature of hot-hole transfer in charge generation. In this report we are probe the role of hot hole transfer in polaron formation, giving important information to the role of hot charge carriers on the way to photocurrent generation in hybrid devices.

Here, we look for evidence of hot hole transfer from photoexcited quantum dots to conjugated polymers by measuring the yield of long-lived charge carriers in polymer/quantum dot hybrids as a function of excitation wavelength. We chose a blend of poly-3-hexylthiophene (P3HT) with PbS quantum dots as our model system, because the comparatively narrow gap of P3HT allows us to spectrally isolate the photoexcitation the quantum dots from the excitation of the polymer over a wider range than would

be possible with previous polymers we have studied.[28] Although blends of larger PbS dots with P3HT show little evidence of photoinduced charge transfer,[29] smaller-sized (larger-gap) PbS dots, when treated with the appropriate ligand exchange protocols (see SI), do produce measurable yields of long-lived charge under photoexcitation, making them a useful system for our study.

We prepared samples for PIA by spin coating blend solutions of P3HT and PbS quantum dots in a nitrogen glovebox and treating them with 10 mM 3-mercaptopropionic acid (MPA) solution (see supporting information section 1). We selected MPA to passivate PbS because of its reported high carrier mobility-lifetime product.[30, 31] Furthermore, we selected a sample that exhibited minimal photoluminescence (PL) because the residual PL signal from smaller-sized PbS quantum dots can interfere with the P3HT polaron signal (see the supporting information, section 1).

We used PIA to probe the long-lived excited states that were formed following the photoexcitation of P3HT/PbS blends. PIA is a pump-probe technique measuring changes in optical transmission due to the formation of long-lived excited states such as polarons with lifetimes on the micro-to-millisecond timescale.[29, 32-34] To probe the polaron population as a function of pump photon energy, we used five LEDs as pump sources: 447 nm (2.77 eV), 660 nm (1.88 eV), 740 nm (1.68 eV), 850 nm (1.46 eV), and a 950 nm (1.31 eV). (Experimental details are included in the supporting information section 2.)

Figure 1 shows the UV-Vis spectra of the P3HT polymer film, the PbS quantum dot solution, and the P3HT/PbS film. Fig. 1 also shows the normalized spectra of the various pump sources used in these experiments. Notably, the 740 nm, 850 nm, and 950 nm LEDs have virtually no overlap with the P3HT absorption spectrum and thus selectively excite the PbS dots.

Figure 2 shows normalized photoinduced absorption spectra of the P3HT/PbS film taken in the NIR region with each of the five different pumps. The broad induced absorption feature with a shoulder at around 1.25 eV is characteristic of P3HT polarons,[29, 32] and matches the polaron spectrum of a control P3HT/fullerene blend (see SI-2.4). Fig. 2 also shows that regardless of pump excitation energy, the shape of the PIA spectra are identical, indicating that we are probing the same polaron species.

Since PIA signal magnitude is dependent upon the absorbed excitation flux, it is important to compare $\frac{\mathrm{dT}}{\mathrm{T}}$ data between different pump energies at the same absorbed photon flux. For each pump wavelength we systematically varied the excitation flux and determined the corresponding polaron yield from the PIA signal at 1050 nm. Figure 3 is the key figure of this manuscript and plots the fractional change in probe beam transmission at 1050 nm (1.18 eV) as a function of absorbed photon flux (incident photon flux corrected by sample absorption), which we determined in the following manner:

$$\Phi_{\mathrm{abs}} = \int \Phi_{\mathrm{P}}(\lambda)\left[1\text{-}10^{-\mathrm{OD}(\lambda)}\right]\mathrm{d}\lambda$$

where Φ_{abs} is the number of photons absorbed per second, $\Phi_{\mathrm{P}}(\lambda)$, is the photon flux coming from the LED at a given wavelength, and *OD(λ)* is the wavelength-dependent optical density as measured from the sample's absorbance spectrum.

In other words, Figure 3 shows the intensity dependence of the polaron signal for all five studied pump wavelengths as a function of the number of photons absorbed by the sample each second. Per absorbed photon, the longest wavelength excitation is the least effective at generating long-lived polarons, and the shortest wavelength excitation is the most effective. The other wavelengths fall in between, with the polaron signal at a given absorbed flux increasing monotonically as the energy of the pump photons increases.

In order to analyze the data more quantitatively, we performed a global power law fit of PIA signal vs. absorbed photon flux of the form:

$$\frac{\mathrm{dT}}{\mathrm{T}} = \mathrm{A}(\Phi_{\mathrm{abs}})^{\mathrm{b}}$$

where A and b serve as fit parameters and b is constrained to fall between 0.5 and 1. We chose this fit function based on the expected dependence of the quasi-CW PIA signal on the polaron generation rate (absorbed photon flux).[35-37] For purely 1st order recombination, dT/T should be linear in Φ_{abs} photon flux (b=1.0).[36] For purely 2nd order (bimolecular recombination) dT/T should scale as a power law in Φ_{abs} with b=0.5.[37] In a dispersive system the behavior is more complicated.[35] A global fit over multiple data sets (see SI) yields b=0.59, describes the data in Fig. 3 well, and is also in good agreement with the intensity dependence previously reported for a different conjugated polymer/PbS blend.[28] The power law exponent of 0.59 is close to the value of 0.5 expected for a 2nd order process, and suggests that bimolecular carrier recombination is the primary decay pathway in these samples under PIA conditions.

Consistent with this analysis, we assume that the measured polarons are primarily decaying via bimolecular processes, in which case the polaron generation rate, *g*, will be proportional to the square of the observed dT/T signal.[36, 37] Fig. 4 plots the normalized generation rate *g* (the square of the prefactor *A* from the fits in Fig. 3) as a function of pump energy. We see that the generation rate increases monotonically with pump energy, as expected based on the visible trends from Fig. 3. Since the three lowest energy pump wavelengths are not absorbed by the P3HT, we conclude that hole transfer from the quantum dots to the polymer is strongly dependent on the energy of the absorbed photon. This result indicates that hole transfer must be taking place, at least at some of the P3HT/PbS interfaces, on timescales faster than the carrier cooling times of ~tens of ps that have been measured for PbS dots.[38, 39] Our interpretation of Fig. 3 in terms of hot hole transfer is thus consistent with the sub-ps hole transfer times that Siebbeles and co-workers have previously measured in PbS/P3HT blends (albeit with different surface ligands).[40]

Moving to the higher pump-photon energies in Fig. 4, the data suggest a further increase in the relative generation rate when both the quantum dots and the polymer are photoexcited. Although we can only speculate with the current dataset, we suggest that this trend could result from a combination of hot hole transfer, and a more favorable rate of polymer-to-quantum dot electron transfer compared with quantum-dot-to-polymer hole transfer.[28]

To conclude, in a model P3HT/PbS blend we observe increasing polymer polaron yields with increasing pump-photon energy, a result that we interpret as being due to the transfer of non-thermalized holes from the photoexcited quantum dots to the polymer host. This finding might help explain the wavelength dependent internal quantum efficiencies that have been previously reported for polymer/PbS blend solar cells,[8] and is consistent with hole transfer occurring faster than the typical intraband carrier relaxation times in surface-treated PbS dots in this blends. In addition to explaining the performance characteristics of hybrid bulk heterojunction solar cells, we expect these results might further be useful in designing organic/inorganic heterojunctions for use in exciton fission and carrier multiplication schemes where there may be a need to optimize relative charge transfer and carrier cooling rates.

Acknowledgements
This work was primarily supported by DOE BES DE-FG02-07ER46467.

See Appendix 2 for futher details: <PbS quantum dot synthesis, sample fabrication, sample photoluminescence are included in the first section. Section 2 has experimental details of the PIA data in Fig 3 and has figures that show (1)repeated measurements for the figure and their associated fit equations , (2)the dependence of PIA signal on the pump chopping frequency, and (3)comparison of the PbS/P3HT PIA spectrum to a PCBM/P3HT spectrum. Section 3 provides details of a verification experiment that uses a chopper and a range of ND filters to ensure the data in Fig 3 is independent of electronic artifacts.> This material is available free of charge via the Internet at http://pubs.acs.org

Figures for Chapter 4

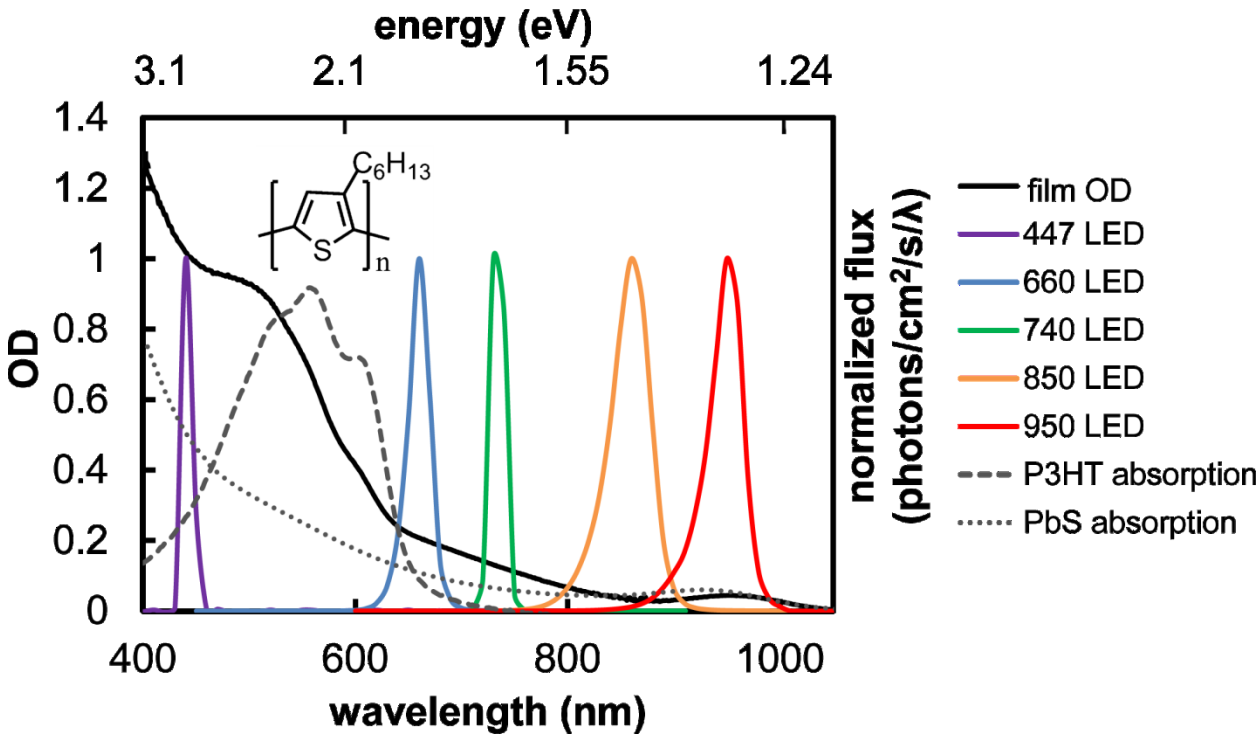

Figure 1 UV Vis absorption spectra of a P3HT film (gray dashed line), PbS quantum dots in solution (dotted line) and P3HT/PbS thin film blend (solid black line). The PbS quantum dots used for these experiments had a quantum-confined exciton peak at 925 nm in solution. The colored peaks are the (normalized) spectra of the various pump LEDs. From left to right the pumps are 447 nm with a 450 nm bandpass filter, 660 nm, 740 nm with a 740 nm bandpass filter, 850 nm, and finally 950 nm. We note the P3HT absorption does not overlap significantly with the 740, 850 or 950 nm pumps.

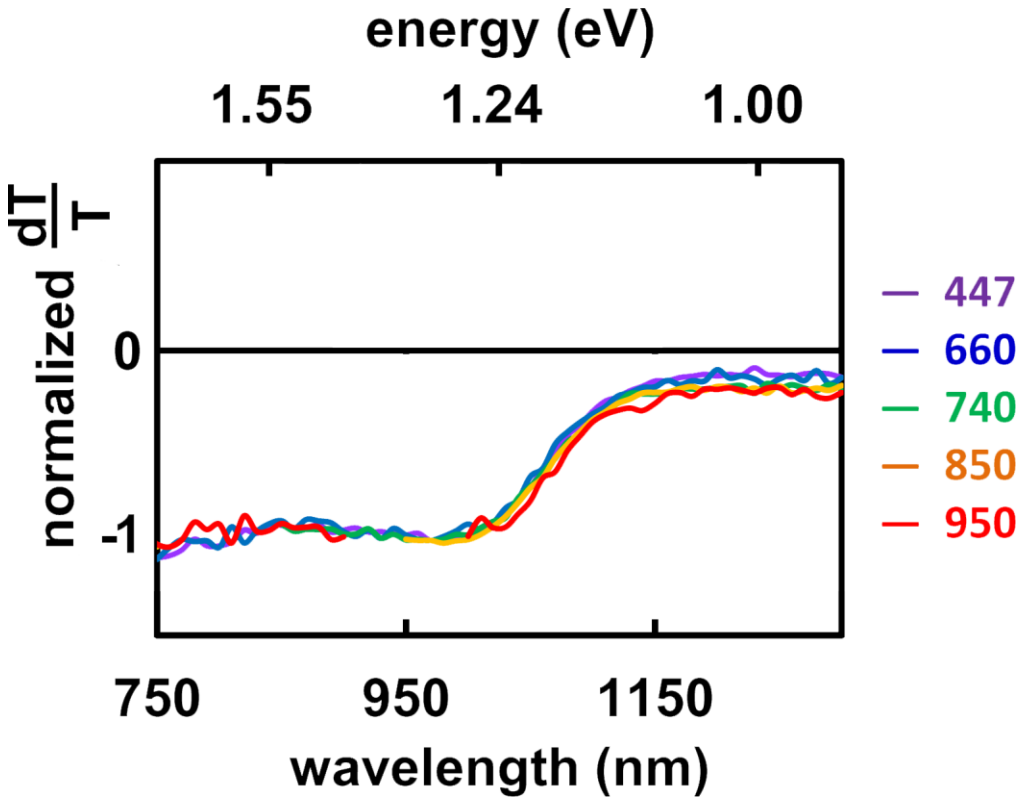

Figure 2 X-channel (in phase) PIA spectra for a P3HT/PbS blend excited with 5 different pump energies. The broad photoinduced absorption peak from 950 to 1150 nm is the well identified polaron peak of P3HT. The spectral shape of the PIA feature is independent of excitation energy.

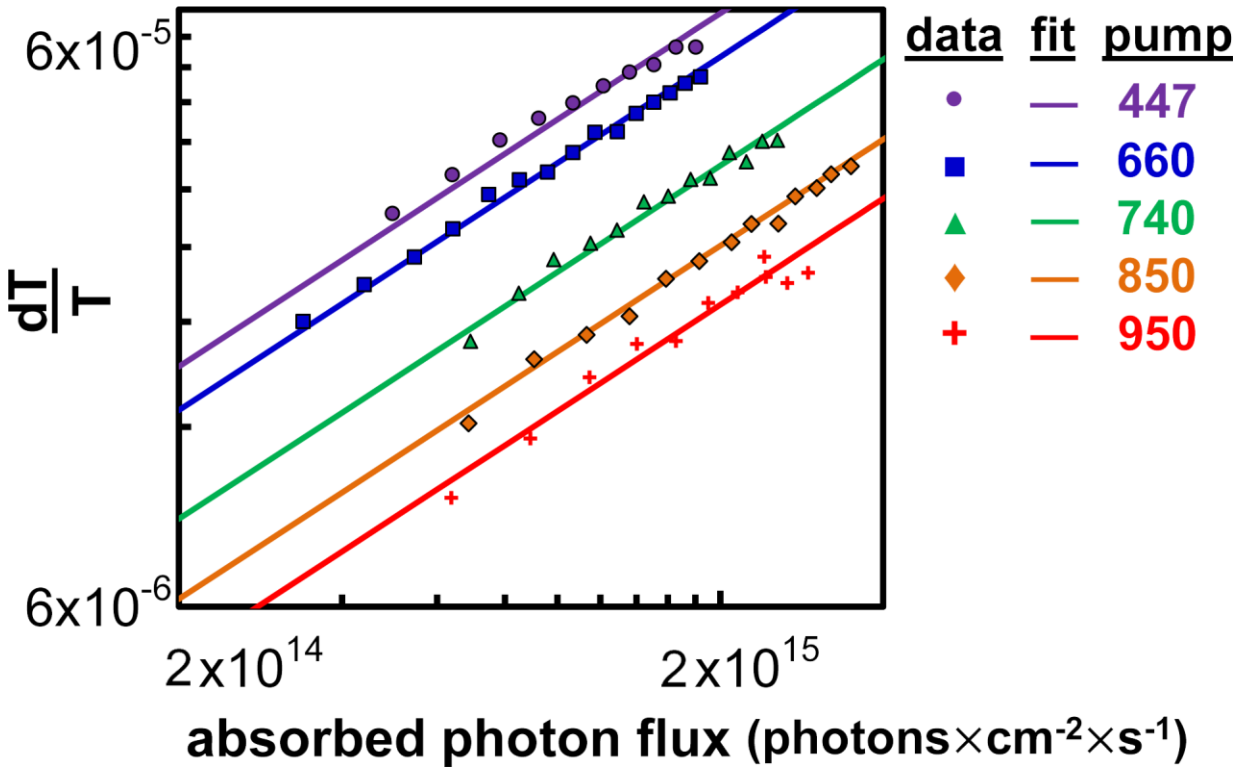

Figure 3 Intensity dependence of the PIA polaron signal at 1050 nm (1.18 eV) for different pump energies as a function of absorbed photon flux. The straight lines are fits to the data as explained in the text. The fit equations are as follows: $\phi_{447} = 7.25 \times 10^{-15} \left(\frac{dT}{T}\right)^{0.59}$, $\phi_{660} = 6.13 \times 10^{-15} \left(\frac{dT}{T}\right)^{0.59}$, $\phi_{740} = 4.03 \times 10^{-15} \left(\frac{dT}{T}\right)^{0.59}$, $\phi_{850} = 2.96 \times 10^{-15} \left(\frac{dT}{T}\right)^{0.59}$ and $\phi_{950} = 2.36 \times 10^{-15} \left(\frac{dT}{T}\right)^{0.59}$. For clarity we display only one data set for each pump excitation wavelength however the fits are best fits to the entire set of repeated measurements with each pump LED. For additional fitting details and full data set see supporting information.

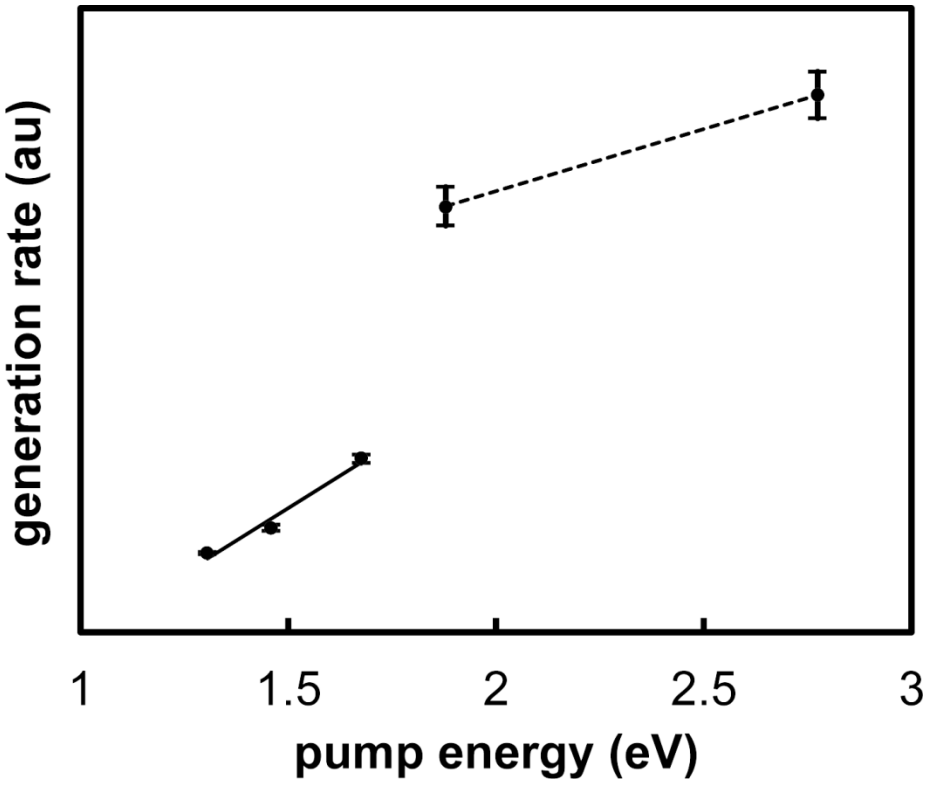

Figure 4 Polaron generation rate (proportional to $\left(\frac{dT}{T}\right)^2$) plotted vs. pump energy. The symbols are average values of two sets of data, and the error bars are the standard deviations. The dashed fit line from 1.7 eV to 3 eV indicates the regime where both the polymer and quantum dots absorb. The solid fit line below 1.7 eV indicates where only the quantum dots are contributing to the film absorption.

1. J. Y. Kim, O. Voznyy, D. Zhitomirsky and E. H. Sargent, *Advanced Materials*, 2013, **25**, 4986-5010.
2. S. ten Cate, Y. Liu, J. M. Schins, M. Law and L. D. A. Siebbeles, *The Journal of Physical Chemistry Letters*, 2013, **4**, 3257-3262.
3. J. J. Choi, Y. F. Lim, M. B. Santiago-Berrios, M. Oh, B. R. Hyun, L. F. Sung, A. C. Bartnik, A. Goedhart, G. G. Malliaras, H. D. Abruna, F. W. Wise and T. Hanrath, *Nano Letters*, 2009, **9**, 3749-3755.
4. J. J. Choi, W. N. Wenger, R. S. Hoffman, Y. F. Lim, J. Luria, J. Jasieniak, J. A. Marohn and T. Hanrath, *Advanced Materials*, 2011, **23**, 3144-+.
5. S. B. Darling and F. You, *RSC Advances*, 2013, **3**, 17633-17648.
6. K. Vandewal, S. Himmelberger and A. Salleo, *Macromolecules*, 2013, **46**, 6379-6387.
7. C. Piliego, M. Manca, R. Kroon, M. Yarema, K. Szendrei, M. R. Andersson, W. Heiss and M. A. Loi, *J. Mater. Chem.*, 2012, **22**, 24411-24416.
8. K. M. Noone, E. Strein, N. C. Anderson, P. T. Wu, S. A. Jenekhe and D. S. Ginger, *Nano Letters*, 2010, **10**, 2635-2639.
9. E. Strein, A. Colbert, S. Subramaniyan, H. Nagaoka, C. W. Schlenker, E. Janke, S. A. Jenekhe and D. S. Ginger, *Energy & Environmental Science*, 2013, **6**, 769-775.
10. M. J. Greaney, S. Das, D. H. Webber, S. E. Bradforth and R. L. Brutchey, *ACS Nano*, 2012, **6**, 4222-4230.
11. S. Dayal, N. Kopidakis, D. C. Olson, D. S. Ginley and G. Rumbles, *Nano Lett.*, 2010, **10**, 239-242.

12. M. M. Lee, J. Teuscher, T. Miyasaka, T. N. Murakami and H. J. Snaith, *Science*, 2012, **338**, 643-647.
13. M. Z. Liu, M. B. Johnston and H. J. Snaith, *Nature*, 2013, **501**, 395-+.
14. P. K. Nayak, K. L. Narasimhan and D. Cahen, *Journal of Physical Chemistry Letters*, 2013, **4**, 1707-1717.
15. S. D. Dimitrov and J. R. Durrant, *Chemistry of Materials*, 2013.
16. T. M. Clarke and J. R. Durrant, *Chemical Reviews*, 2010, **110**, 6736-6767.
17. J.-L. Brédas, J. E. Norton, J. Cornil and V. Coropceanu, *Accounts of Chemical Research*, 2009, **42**, 1691-1699.
18. A. Rao, P. C. Y. Chow, S. Gelinas, C. W. Schlenker, C.-Z. Li, H.-L. Yip, A. K. Y. Jen, D. S. Ginger and R. H. Friend, *Nature*, 2013, **500**, 435-439.
19. G. Grancini, M. Maiuri, D. Fazzi, A. Petrozza, H. J. Egelhaaf, D. Brida, G. Cerullo and G. Lanzani, *Nature Materials*, 2013, **12**, 29-33.
20. N. Bansal, L. X. Reynolds, A. MacLachlan, T. Lutz, R. S. Ashraf, W. M. Zhang, C. B. Nielsen, I. McCulloch, D. G. Rebois, T. Kirchartz, M. S. Hill, K. C. Molloy, J. Nelson and S. A. Haque, *Scientific Reports*, 2013, **3**.
21. X. Y. Zhu, Q. Yang and M. Muntwiler, *Accounts of Chemical Research*, 2009, **42**, 1779-1787.
22. A. E. Jailaubekov, A. P. Willard, J. R. Tritsch, W. L. Chan, N. Sai, R. Gearba, L. G. Kaake, K. J. Williams, K. Leung, P. J. Rossky and X. Y. Zhu, *Nature Materials*, 2013, **12**, 66-73.
23. W. A. Tisdale, K. J. Williams, B. A. Timp, D. J. Norris, E. S. Aydil and X. Y. Zhu, *Science (Washington, DC, U. S.)*, 2010, **328**, 1543-1547.
24. H. Ohkita, S. Cook, Y. Astuti, W. Duffy, S. Tierney, W. Zhang, M. Heeney, I. McCulloch, J. Nelson, D. D. C. Bradley and J. R. Durrant, *Journal of the American Chemical Society*, 2008, **130**, 3030-3042.
25. S. D. Dimitrov, A. A. Bakulin, C. B. Nielsen, B. C. Schroeder, J. Du, H. Bronstein, I. McCulloch, R. H. Friend and J. R. Durrant, *Journal of the American Chemical Society*, 2012, **134**, 18189-18192.
26. V. I. Arkhipov, P. Heremans and H. Bässler, *Applied Physics Letters*, 2003, **82**, 4605.
27. Y. Yang, W. Rodríguez-Córdoba, X. Xiang and T. Lian, *Nano Letters*, 2011, **12**, 303-309.
28. A. E. Colbert, E. M. Janke, S. T. Hsieh, S. Subramaniyan, C. W. Schlenker, S. A. Jenekhe and D. S. Ginger, *Journal of Physical Chemistry Letters*, 2013, **4**, 280-284.
29. K. M. Noone, N. C. Anderson, N. E. Horwitz, A. M. Munro, A. P. Kulkarni and D. S. Ginger, *ACS Nano*, 2009, **3**, 1345-1352.
30. K. S. Jeong, J. Tang, H. Liu, J. Kim, A. W. Schaefer, K. Kemp, L. Levina, X. Wang, S. Hoogland, R. Debnath, L. Brzozowski, E. H. Sargent and J. B. Asbury, *ACS Nano*, 2012, **6**, 89-99.
31. A. H. Ip, S. M. Thon, S. Hoogland, O. Voznyy, D. Zhitomirsky, R. Debnath, L. Levina, L. R. Rollny, G. H. Carey, A. Fischer, K. W. Kemp, I. J. Kramer, Z. Ning, A. J. Labelle, K. W. Chou, A. Amassian and E. H. Sargent, *Nat. Nanotechnol.*, 2012, **7**, 577-582.
32. K. M. Noone, S. Subramaniyan, Q. Zhang, G. Cao, S. A. Jenekhe and D. S. Ginger, *J. Phys. Chem. C*, 2011, **115**, 24403-24410.
33. D. S. Ginger and N. C. Greenham, *Synthetic Metals*, 1999, **101**, 425-428.
34. D. S. Ginger and N. C. Greenham, *Physical Review B*, 1999, **59**, 10622-10629.
35. M. Wohlgenannt, E. Ehrenfreund and Z. V. Vardeny, in *Photophysics of Molecular Materials: From Single Molecules to Single Crystals*, ed. G. Lanzani, Wiley-VCH, Weinheim, 2006, ch. 5, pp. 183-259.
36. C. Botta, S. Luzzati, R. Tubino, D. D. C. Bradley and R. H. Friend, *Physical Review B*, 1993, **48**, 14809-14817.
37. G. Dellepiane, C. Cuniberti, D. Comoretto, G. F. Musso, G. Figari, A. Piaggi and A. Borghesi, *Physical Review B*, 1993, **48**, 7850-7856.

38. R. J. Ellingson, M. C. Beard, J. C. Johnson, P. Yu, O. I. Micic, A. J. Nozik, A. Shabaev and A. L. Efros, *Nano Letters*, 2005, **5**, 865-871.
39. J. T. Stewart, L. A. Padilha, M. M. Qazilbash, J. M. Pietryga, A. G. Midgett, J. M. Luther, M. C. Beard, A. J. Nozik and V. I. Klimov, *Nano Lett.*, 2012, **12**, 622-628.
40. S. ten Cate, J. M. Schins and L. D. A. Siebbeles, *ACS Nano*, 2012, **6**, 8983-8988.

Chapter 5: Conclusion

This dissertation ends with a look toward the future as we consider how to extend and expand upon the research discussed throughout this work.

Chapter three provides evidence that polymer/quantum dot devices can behave as bulk heterojunctions where carriers are transferred at the polymer/quantum dot interface. Other devices behave as schottky diodes where the drive for charge separation comes from the alignment of the quantum dot Fermi level to the metal workfunction. With the schottky diode devices it appears that some polymers--notably PSOTT-- undergo considerable energy-transfer with the PbS quantum dots, in contrast with the photoinduced charge separation processes observed in the other blends. However it is not clear why PSOTT behaves differently from the other two studied polymers. As discussed in the paper, PSOTT differs from PDTPQx-HD and PPEHTT in two interesting ways: (1)it has linear rather than branched side chains and (2)it has the most shallow ground state ionization energy, nearly matching conduction band energy of the PbS quantum dots. In order to understand the behavior of PSOTT new polymers would need to be fabricated with side chains that match those on PPEHTT and PDTPQx-HD and backbones that match PSOTT. Using the spectroscopic techniques found in chapter three, blends of PbS quantum dots with these new polymers could be probed to see if charge transfer occurs with the new polymers. The result would let us know what aspect of PSOTT causes the observed energy-transfer behavior.

Chapter four provides evidence that the polaron yield rises with increasing excitation energy in blends of P3HT/PbS quantum dots. This initial study provides rich ground for additional research. The final figure suggests that there might be two generation rate regimes: the generation rate when only the PbS quantum dots are excited and another rate when both polymer and quantum dots are excited. To verify this suggestion the sample needs to be probed with additional excitation energies, particularly where both polymer and quantum dot can absorb the excitation light. Collaboration using ultrafast spectroscopy would be very useful, as it would allow us to study timescales that are faster than the micro-to-millisecond range we can access with PIA, providing access to charge transfer rates as the excitation energy is varied. Also it would be interesting to see if either the bandgap of the quantum dots or the type of ligand treatment influences the polaron yields and generation rates. It also would be interesting to see if this trend might be observed—and if the rate differs from the polymer/quantum rate(s)—for the P3HT/PCBM system over an appropriate excitation range for this system.

Many questions remain concerning polymer/PbS quantum dot solar devices—the field is an exciting one with much growth and depth of understanding in its future.

Appendix 1 for Chapter 3: Charge Generation and Energy Transfer in Hybrid Polymer/Infrared Quantum Dot Solar Cells

Synthesis of Poly[(4,4'-bis(3-(2-hexyl-decyl)dithieno[3,2-b:2',3'-d]pyrrole)-2,6-diyl-alt-(2,5-bis(3-(2-ethyl-hexyl)thiophen-2yl)thiazolo[5,4-d]thiazole)](PPEHTT): The di(trimethyltin)-*N*-(1-hexyldecyl)dithieno[3,2-*b*:30-*d*]-pyrrole (250 mg, 0.34 mmol) and 2,5-Bis-[5-bromo-(2-ethyl-hexyl)-thiophen-2yl]-thiazolo[5,4-d]thiazole (196 mg, 0.34 mmol) and catalyst tris(dibenzylideneacetone)dipalladium (0) (6 mg, 0.07 mmol) and tri-*o*-tolylphosphine (8 mg, 0.027 mmol) in anhydrous chlorobenzene (25 mL) were heated at 125 ^{o}C for 3 days. Then the heating was reduced to 50 $^{\circ}$C. The reaction mixture was poured into 200 mL of methanol containing 5 mL of hydrochloric acid and stirred for 5 h. The dark brown precipitate was collected via filtration, and was further purified by Soxhlet extraction with methanol and hexane. The polymer was further purified by dissolving chloroform and then reprecipitated in methanol. The solid was filtered and dried into vacuum oven for 10 h and collected as a dark brown solid. Yield (260 mg, 81%). ^{1}H NMR ($CDCl_3$, 300 MHz, ppm): 6.31-6.95 (m, 4H), 3.81 (bs, 2H), 2.75 (bs, 4H), 0.81-1.81 (m, 61H). GPC: M_w = 13.46 kDa, M_n = 8.41 kDa, PDI = 1.6.

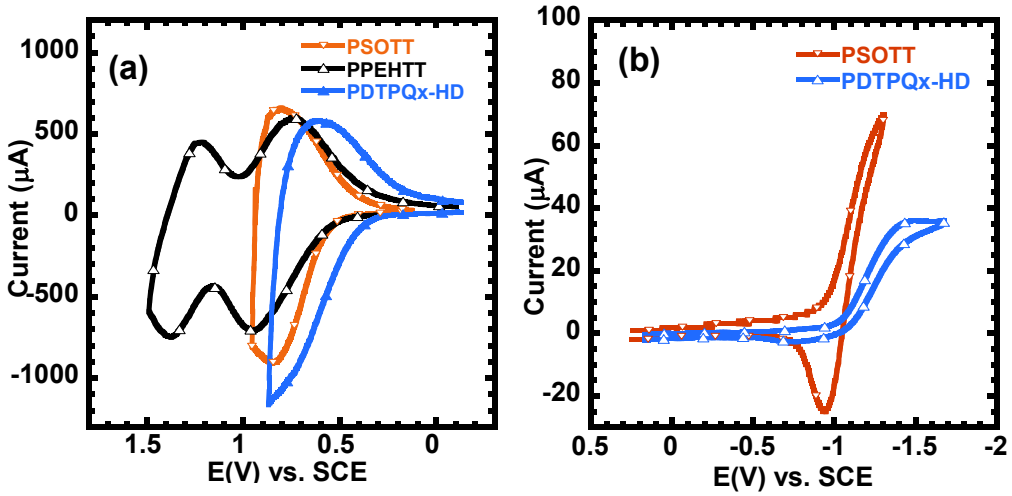

Figure SI.1 Cyclic voltammograms of PSOTT, PPEHTT and PDTPQx thin films in 0.1 M Bu_4NPF_6 solution in acetonitrile at a scan rate of 40 mV/s: (a) oxidation waves and (b) reduction waves.

Additional PIA characterization:

We further characterize the materials by probing neat QD films, polymer/fullerene films and pristine PSOTT polymer films.

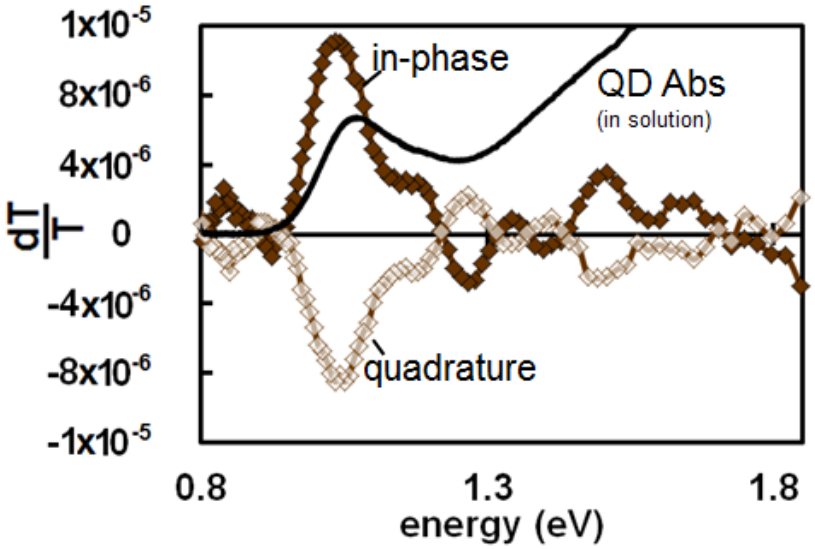

Figure SI.2 Curve with solid brown diamonds is the in-phase photoinduced absorption signal which probes states and white diamonds correspond with quadrature signal taken on a thin film of quantum dots. The quantum dot absorption spectrum is overlayed on the PIA data as a solid black line. PIA on neat PbS quantum dot film shows a bleach feature that corresponds in energy with the QD absorption peak. The bleach feature (particularly in the quadrature signal) can be significantly diminished after the films have been EDT treated.

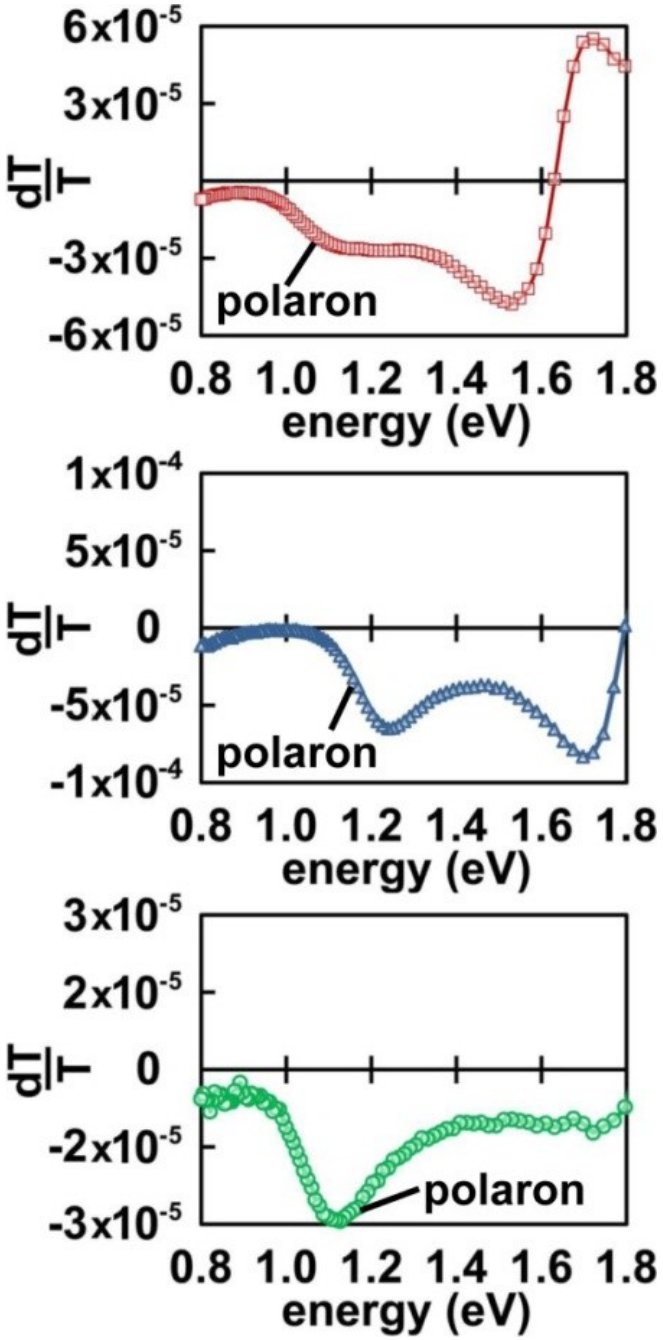

Figure SI.3 PIA signal for PDTPQx-HD, PPEHTT, and PSOTT when blended with fullerene ($PC_{60}BM$ in the case of PDTPQx-HD and PPEHTT and $PC_{71}BM$ in the case of PSOTT). Of particular note, there is a clear long-lived signal for the PSOTT/fullerene blend. The polaron peaks for PDTPQx-HD and PPEHTT match the positions of the peaks in the polymer/PbS blends (main text Fig. 2). While the PSOTT/fullerene blend has a strong peak at ~1.1 eV (above) The PSOTT/PbS blend has no significant long live polaron signal at room temperature (main text Fig. 2).

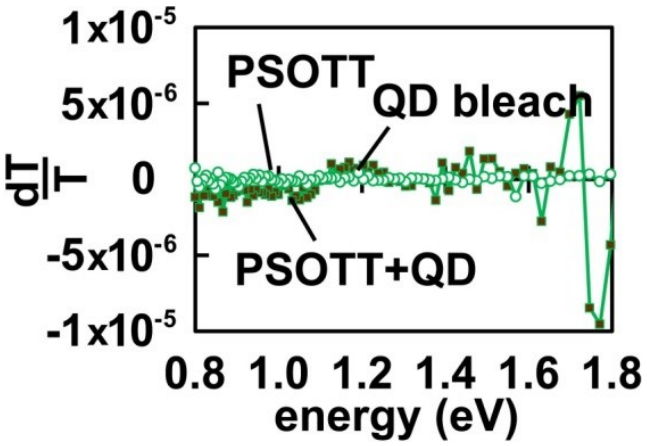

Figure SI.4 For comparison, we overlay PIA spectra of pristine PSOTT with a PSOTT/quantum blend and see comparable signal at room temperature.

Additional device characterization

Schematic Diagram of PSOTT/PbS "Schottky-diode" device

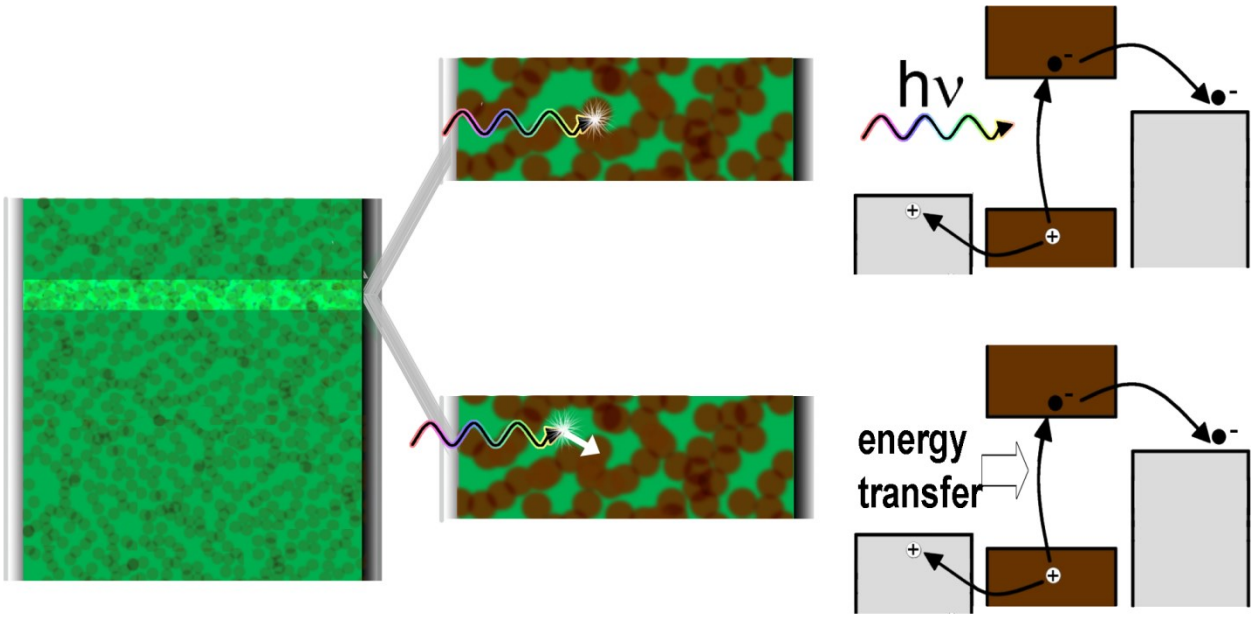

Figure SI.5 Schematic diagram of the PSOTT/quantum dot "Schottky-diode" device. The ITO/PEDOT hole collecting electrode is denoted by a vertical light gray bar. In the active area portion of the drawing, the green represents the PSOTT polymer and the brown circles represent PbS quantum dots. The LiF/Al contact is drawn as a darker gray vertical strip. For clarity, the highlighted horizontal strip in

the device is magnified in the two images in the center of the figure which demonstrate pictorially two routes for generating photocurrent in the Schottky-diode device. In the upper image, a photon is absorbed by a quantum dot, in the manner typical of quantum dot Schottky-diode devices. In the bottom image, the photon is absorbed by the polymer and the energy stored in the polymer excited state is then transferred to the quantum dot. The cartoons to the right of each image depict these two routes schematically.

Additional notes about device fabrication

The thicknesses of the devices reported in Fig. 3 vary between polymers. Although due to limited supply of polymer we did not undertake a systematic thickness optimization for devices, through repeated trials (with varying quantum dot batches and ligand treatments) we saw optimal thickness ranges for the respective polymer/quantum dot blends and consequently tailored further device fabrication to mirror what produced the best results for a particular blend system. We found that PPEHTT/PbS device performance was best with a ~ 60 nm active area thickness and was typically worse with 40 and 80 nm device thicknesses. PDTPQx/PbS blends had poorer performance with thinner active areas (30-40 nm) and generally improved performance with active areas anywhere between 60-100 nm. PSOTT/PbS blends conversely showed the best performance with a thinner (~40 nm) active area and device performance decreased with thicker active areas.

Although device thickness certainly impacts device performance, we found the effect minor compared to the impact of thiol treating the devices. As illustration we show EQE from a PSOTT device that was not EDT treated.

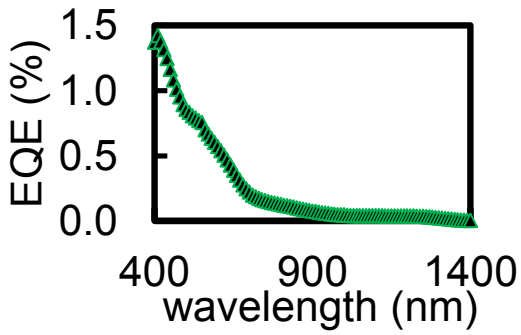

Figure SI.6 a “high performing” EQE spectrum for a PSOTT/PbS device that did not undergo EDT treatment. Photocurrent is more than an order of magnitude lower than for EDT treated devices

In addition to measuring EQE, current-voltage sweeps were also measured for each device as shown in SI.7.

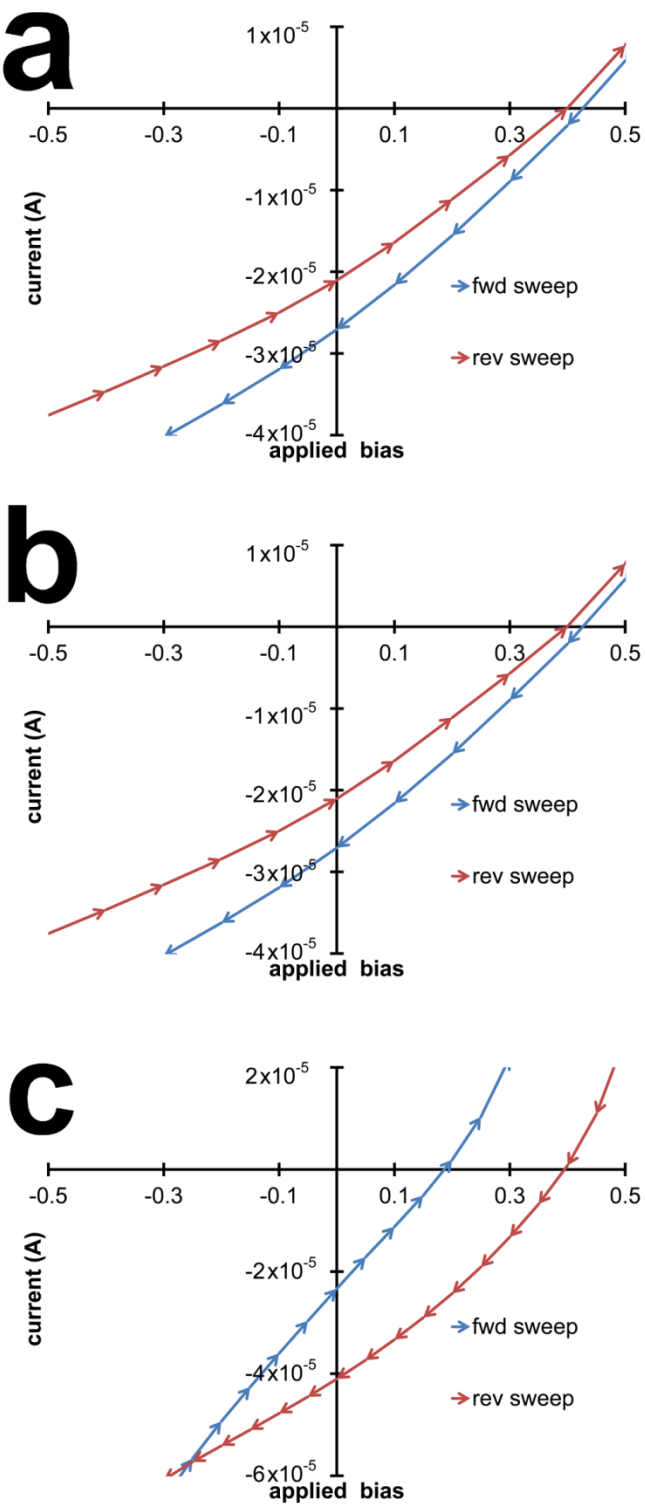

Figure SI.7 IV curves for the three devices in figure 3 of the main text. Following the labeling of figure 3, (a) is PDTPQx/PbS (b) is PPEHTT/PbS and (c) is PSOTT/PbS. All devices were masked so that the illuminated area was 0.018 cm^2. They were swept first from -2 to 2 V (forward sweep, blue data) and then 2 V to -2 V (reverse sweep, red data). Data from both sweeps are included (rather than averaged)

to show the varying degrees of hysteresis. These data were taken using a solar simulator, but the solar simulator intensity and spectral mismatch factors were not properly calibrated. As such the general Voc and FF trends are likely to be correct, but the exact values and short circuit current are not reflective of the true AM1.5 performance and we therefore refrain from quoting efficiency (though these data along with the EQE data in the main text could be used to estimate upper limits for these unoptimized devices.)

Appendix 2 for Chapter 4: Hot hole transfer increases polaron yields in hybrid conjugated-polymer/PbS blends

SI SECTION 1: MATERIAL AND SAMPLE PREPARATION AND CHARACTERIZATION

PbS Nanocrystal Synthesis and Treatment

Colloidal PbS quantum dots were prepared by using a slightly modified method described by Hines and Scholes.[1] All reagents were purchased from Sigma-Aldrich and used without further purification. The lead precursor was prepared by mixing PbO (0.45 g, 2.00 mmol), oleic acid (1.2 g, ~4.25 mmol), and 1-octadecene (ODE) (14 g) in a three-neck flask with a stir bar. The reaction flask was purged with nitrogen and stirred under vacuum at 100 ˚C for at least 1 hour or until the mixture turned clear. The reaction flask was then returned to nitrogen flow and heated to 120 ˚C in preparation for injection of the sulfur precursor.

The sulfur precursor was prepared by combining 210 µL of hexylmethyldisilazane (HMDS) with 4 g of ODE in a separate three-neck flask. This solution was stirred at room temperature under an inert atmosphere for approximately five minutes. The sulfur precursor solution was then injected into the reaction flask via syringe. The injection was done quickly in order to prevent multiple nucleation events from taking place. The heating mantle was immediately switched off after injection and the flask was allowed to cool to 30 ˚C. The PbS quantum dots were precipitated by addition of acetone and centrifuged for 5 min at 2500 rpm. The supernatant was decanted and PbS quantum dots were dissolved in hexanes and then precipitated with methanol. The cleaned product was dried under nitrogen in preparation for the butylamine ligand exchange.

Solution-based ligand exchange

The dried product was dissolved in the proper volume of butylamine (3.7 mL) to make an 80 mg/mL solution. This solution was sonicated for 20 minutes, then precipitated with methanol and centrifuged. The supernatant was decanted and the precipitate was dried under nitrogen. These steps were repeated twice, but isopropanol was used to precipitate the PbS. The precipitate was dried under nitrogen until a constant mass was observed. PbS quantum dots capped with butylamine ligands were dissolved in anhydrous dichlorobenzene to make a solution with a concentration of 200 mg/mL. Concentration was verified using a Cary spectrophotometer and a method previously described by Hens.[2]

Sample Fabrication and Characterization

A 40 mg/mL solution of regioregular P3HT (Rieke Metals) was prepared in anhydrous dichlorobenzene and stirred at 60° C overnight. A blend solution was then prepared by mixing the P3HT and PbS solutions in a 1:9 (w/w) ratio, and stirring at 50° C for at least 4 hrs. The solution was filtered with a 1 µm PTFE filter and spun onto clean glass at 1000 rpm for 8 s, then 1700 rpm for 2 min.

Thin-film ligand exchange

Ligand treatment with 3-mercaptopropionic acid (MPA, Aldrich) was performed on spin-cast films in order to remove insulating oleate and butylamine ligands and passivate the surface as previously described in the literature.[3, 4]

A 10 mM solution of MPA was made by dissolving 4.25 mg MPA in 4 mL of reagent grade methanol. Ligand treatment was performed post-deposition by treating the spin-cast layer with 85 µL of the MPA solution for 30 s, spinning the unreacted excess solution off, and then a subsequent wash with pure methanol. This step was repeated two more times for a total of three post deposition treatments.

Sample OD (see Fig 1 in the main article) was measured in ambient conditions using a Cary UV-Vis-NIR spectrophotometer. Because the sample is exposed to air in order to obtain the spectrum, the absorption was not measured on the sample until after the PIA data was taken. In order to calibrate the number of absorbed photons for each pump, the OD was measured on a film prepared at the same time as the sample with the same solution and under identical conditions.

Sample PL was measured as part of the PIA measurement. It was necessary to measure PL in order to distinguish PIA signal from any sample PL emission signal that also was collected by the detector. The measurement is accomplished as the sample is excited by the pump while the probe light is blocked. For this sample, the detected PL signal was on the order of the noise (anything lower than 1×10^{-6}). The increased noise level for the 740 nm pump is not related to the pump energy but instead is due to increased electrical noise in the detection electronics—the data was collected at a different amplification setting.

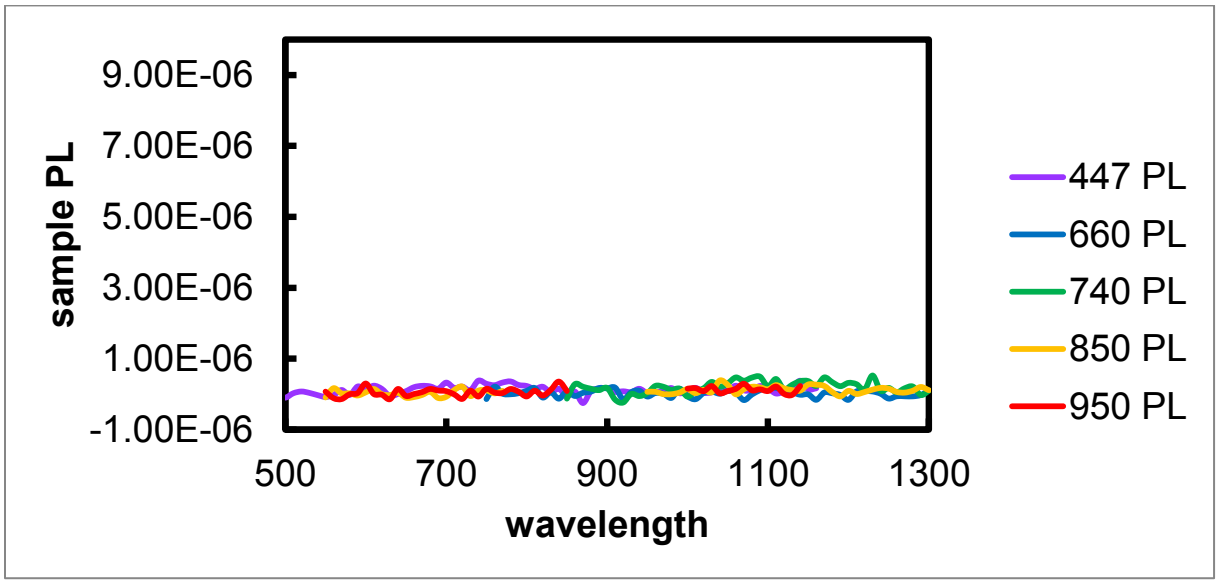

Figure SI-4.1 P3HT/PbS PL intensity measurements for different pump excitations. The detected signal is low, on the order of the noise, suggesting that little/no PL is emitted from the sample regardless of pump energy.

SI SECTION 2: ADDITIONAL EXPERIMENTAL INFORMATION

The sample was pumped using a frequency modulated LED and probed using a monochromated tungsten halogen lamp. To probe the polaron population as a function of pump energy, we used five separate air-cooled LED pumps: a 447 nm LED (Luxeon Rebel, LXML-PR01), a 660 nm LED (LEDEngin, LZ4-00R200), a 740 nm LED (LEDEngin, LZ4-00R300), a 850 nm LED (LEDEngin, LZ4-00R400), and a 950 nm LED (OSRAM Opto Semiconductors, SFH 4239). Pump spectral profiles for 447 nm and 740 nm were narrowed using bandpass filters (Thorlabs, FB450-10 and FB740-10).

Standard lock-in techniques were used to obtain PIA data and consequently all pump illumination on the sample was modulated as described previously.[5-7] Note, the $\frac{dT}{T}$ signal was collected at 1050 nm which falls on the shoulder of the polaron signal in order to measure all pumps at the same probe wavelength (see SI-2.4).

Pump light intensity calibration when electronically modulating the pump

LED pump light intensity was calibrated using a Si photodiode with a known responsivity, sweeping the current through each LED between 100-500 mA, and monitoring the photocurrent from the diode using a Keithley 2400. Neutral density filters (Thorlabs, NE520A or NE530A) were used to ensure the linear response of the diode. The diode was masked to match the area of photoinduced absorption on the sample. Pump light from all LED sources was focused such that it illuminated a larger area of the sample than the probe, consequently ensuring that the area of photoinduced absorption was dictated by the size of the probe beam and remained constant in both size and location as the pump sources were varied. The calibration data provided equations to describe pump photon flux as a function of the current through the LED

$$\Phi_P = P\frac{\lambda}{hc} = \frac{I}{\sigma}\frac{\lambda}{hc}$$

where P is power, h is Planck's constant, c is the speed of light, σ is the responsivity of the Si photodiode and I is calculated using the fit from the calibration data. Calibration data for all pumps are displayed below (Fig SI-2.1)

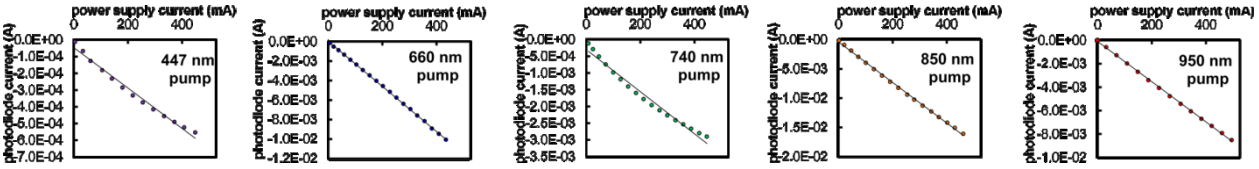

Figure SI-5.1 shows the relationship between current through the Si photodiode and current through the pump for all five pumps. Data were adjusted to account for the neutral density filter used to ensure a linear response on the Si photodiode. We determined that the slight nonlinearities seen in the 447 nm and 740 nm pumps are due to the LED modulation at higher voltages. They do not indicate that the Si photodiode is no longer responding linearly. This was determined by changing the modulation to 1 Hz and observing a linear response across the voltage sweep and confirmed by consistently measuring the non-linear response at high voltages when decreasing the transmitted light intensity via layered ND filters.

Verification of $\frac{dT}{T}$ vs absorbed photon measurements

To demonstrate the range of variation in PIA signal, all measurements were verified through repetition (Figure SI-2.2).

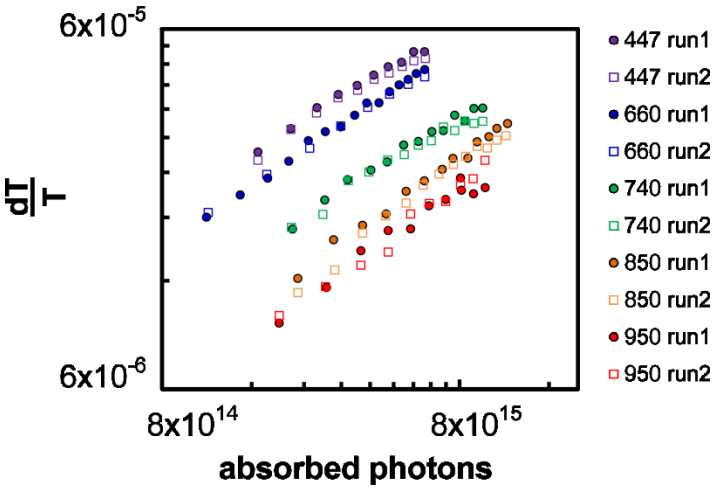

Figure SI-2.2 shows the spread in signal (• and □) for all pumps and demonstrates that the variations in PIA signal for a single pump are smaller than the variation in signal as the pump energy is changed.

As discussed in the main article, a global fit was performed using all the data. The fits for run 1 (closed circles in SI-2.2) are included in the main article. The fits for run 2 (open squares) are as follows: $\phi_{447} = 7.72 \times 10^{-14} \left(\frac{dT}{T}\right)^{0.59}$, $\phi_{660} = 6.31 \times 10^{-14} \left(\frac{dT}{T}\right)^{0.59}$, $\phi_{740} = 4.49 \times 10^{-14} \left(\frac{dT}{T}\right)^{0.59}$, $\phi_{850} = 3.09 \times 10^{-14} \left(\frac{dT}{T}\right)^{0.59}$ and $\phi_{950} = 2.54 \times 10^{-14} \left(\frac{dT}{T}\right)^{0.59}$.

Polaron decay dynamics

Figure SI-2.3 shows the dependence of PIA signal on pump chopping frequency when probed at 1050 nm. This technique has been discussed previously.[5] As displayed in figure SI-2.3 below, regardless of pump energy, we observe nearly identical decay dynamics. This indicates that we are probing the same long lived spectral feature for each pump and that the hot holes do not impact the ratio of geminate to bimolecular recombination on a micro-to-millisecond timescale.

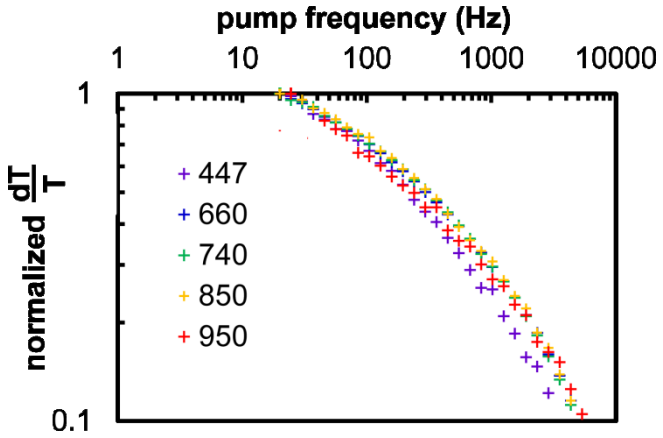

Figure SI-2.3 reports nearly identical polaron decay dynamics for all pump energies as the modulation frequency is varied.

PIA signal for P3HT/fullerene blend

The PIA signal measured in the polymer/quantum dot blend is due to the polaron on the P3HT polymer. We determine this by comparing the P3HT/PbS spectrum to a P3HT/PCBM spectrum and find that the spectral shapes are in good agreement, notably, that the PIA spectral feature from 900-1100 nm in the polymer/quantum dot blend mirrors the assigned polaron feature in the polymer/fullerene blend. As observed in other polymer/quantum dot blends, we measure flatter spectra from 650-900 nm as compared to what is measured in a sister polymer/fullerene blend.

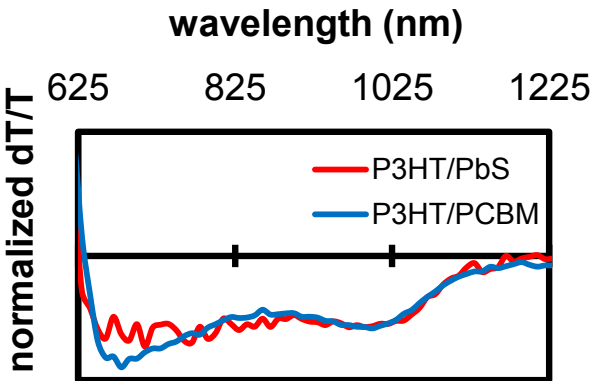

Figure SI-2.4 reports a PIA signal for the P3HT/quantum dot blend that matches the assigned polaron signal for for P3HT/PCBM

SECTION 3: MODULATING MECHANICALLY—A VERIFICATION EXPERIMENT

A mechanical chopper (Stanford Research Systems, SR540) was used to modulate the pump light and light intensity was varied using neutral density filters (Thorlabs, NE501A-NE520A). The spectral linewidth of all pumps was narrowed with bandpass filters (Thorlabs, FB450-10, FB660-10, FB740-10, FB850-10, and FB950-10). The use of the 950 nm bandpass filter allowed us to directly observe changes in intensity at the polaron peak (1000 nm).

Pump light intensity calibration when mechanically modulating the pump

LED pump light intensity was calibrated using a Si photodiode with a known responsivity. We maintained a constant current through the LED and varied the intensity using a range of neutral density filters (Thorlabs, NE501A-520A). Using this chopper/ND filter method ensures the data in Fig 3 in the main article is independent of electronic artifacts. As before the current through the diode was monitored with a Keithley 2400 and the diode was masked to match the area of photoinduced absorption on the sample.

Experimental Data

We show equivalent figures for the verification experiment as are given in the main article.

First, figure SI-3.1a overlays each normalized pump intensity profile over the absorption of the P3HT/PbS sample. Absorption of neat P3HT and PbS quantum dots are displayed as dashed lines. Upon ensuring that the sample absorbed the same number of photons at all pump energies, PIA spectral scans were collected. Figure SI-3.1b shows the total collected PIA signal, R, ($\mathrm{R} = \sqrt{(\mathrm{in})^2 + (\mathrm{quad})^2}$ where *in* is the "in-phase" signal and *quad* is the "quadrature" signal from the lock-in). We verify that the polaron signal increases as the pump energy increases. We also verify (Figure SI-3.1c) this rise in signal (♦) by monitoring the polaron peak (1000 nm) and using neutral density filters to modify the light intensity from the pump. These measurements were then repeated twice (□ and +) to give the spread in the measured signal. Although the 660, 740, and 850 nm pump data all lie close to each other there is still a clear rise in signal as the quantum dots in the sample move from being excited by 950 nm illumination through 740 nm illumination.

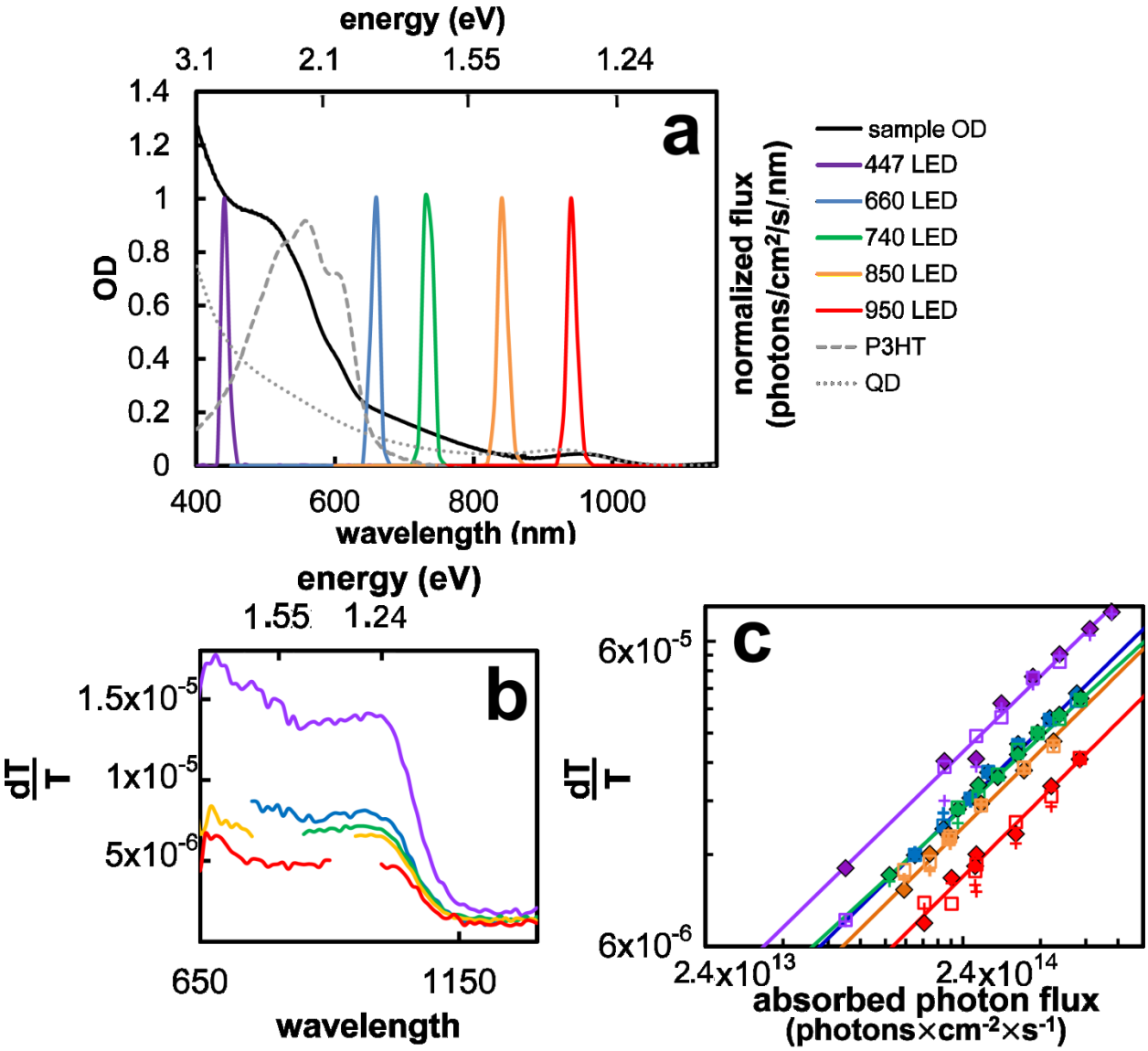

Figure SI-3.1 a overlays each normalized pump intensity profile over the absorption of the P3HT/PbS sample (solid black line). All pumps were equipped with bandpass filters. Absorption of neat P3HT and PbS quantum dots are displayed as dashed lines. **Figure SI-3.1b** shows R data for each pump that was taken such that the sample constantly absorbed the same number of photons regardless of the pump energy. **Figure SI-3.1c** Measured changes in PIA signal at the polaron peak (1000 nm) using neutral density filters to modify the light intensity from the pump. These measurements were taken once (♦) then repeated twice (□ and +) to give the spread in the measured signal.

1. M. A. Hines and G. D. Scholes, *Advanced Materials*, 2003, **15**, 1844-1849.
2. I. Moreels, K. Lambert, D. Smeets, D. De Muynck, T. Nollet, J. C. Martins, F. Vanhaecke, A. Vantomme, C. Delerue, G. Allan and Z. Hens, *Acs Nano*, 2009, **3**, 3023-3030.
3. A. G. Pattantyus-Abraham, I. J. Kramer, A. R. Barkhouse, X. Wang, G. Konstantatos, R. Debnath, L. Levina, I. Raabe, M. K. Nazeeruddin, M. Gratzel and E. H. Sargent, *Acs Nano*, 2010, **4**, 3374-3380.

4. A. H. Ip, S. M. Thon, S. Hoogland, O. Voznyy, D. Zhitomirsky, R. Debnath, L. Levina, L. R. Rollny, G. H. Carey, A. Fischer, K. W. Kemp, I. J. Kramer, Z. Ning, A. J. Labelle, K. W. Chou, A. Amassian and E. H. Sargent, *Nat. Nanotechnol.*, 2012, **7**, 577-582.
5. K. M. Noone, S. Subramaniyan, Q. Zhang, G. Cao, S. A. Jenekhe and D. S. Ginger, *J. Phys. Chem. C*, 2011, **115**, 24403-24410.
6. K. M. Noone, E. Strein, N. C. Anderson, P. T. Wu, S. A. Jenekhe and D. S. Ginger, *Nano Letters*, 2010, **10**, 2635-2639.
7. E. Strein, A. Colbert, S. Subramaniyan, H. Nagaoka, C. W. Schlenker, E. Janke, S. A. Jenekhe and D. S. Ginger, *Energy & Environmental Science*, 2013, **6**, 769-775.